SEISMIC ARRAYS FOR THE IMAGING OF ALLUVIAL DEPOSITS AND MONITORING ENGINEERING SYSTEMS

By

ESRA AK

A thesis submitted in partial fulfillment of

the requirements for the degree of

MASTER OF SCIENCE

(GEOLOGICAL ENGINEERING)

At the

UNIVERSITY OF WISCONSIN – MADISON

2019

LIST OF FIGURES

LIST OF TABLES

Chapter 1: Motivation and Organization of the Thesis

The use of high-density seismic sensor arrays creates an opportunity to image the near surface using high-resolution algorithms, evaluate dynamic properties of shallow deposits, and monitor the usage and assess the health of the geological and civil infrastructure. But this significant number of opportunities comes with a cost. The datasets from high-density seismic sensor arrays are extensive and complex interpretation algorithms are needed to find signals of interests that are embedded in noisy records.

This thesis presents three sets of studies aimed at improving the interpretation and evaluation of process and events from an extensive collection of data collected during the PoroTomo project. The PoroTomo project deployed seismic sensor arrays, monitored active and passive seismic signals, and analyzed data as part of a large technology demonstration study aimed at imaging a geothermal field. PoroTomo used to sites during the survey: Garner Valley (Southern California) and Brady Hot Springs (Northwestern Nevada). In those sites, the research team collected over 50 TB of seismic data (with Nodal geophone arrays and distributed acoustic sensing -DAS- arrays), and while a significant number of studies and papers have been completed, many more studies can still be achieved.

This thesis presents three research studies with the intent of capturing more processes sensed by the seismic distributed arrays. The three research studies are organized into three chapters. Chapters Two and Three deal with the interpretation of active and passive seismic sources at Brady Hot Springs and collected with the nodal geophone array. These two chapters analyzed active and passive seismic data to further the results needed for the high-resolution imaging of the subsurface by extending the arrival times to S-wave arrivals and by determining

the depth to bedrock at Brady Hot Springs. Chapter Four used traffic noise as sources of elastic waves in the DAS arrays both in Garner Valley and Brady Hot Springs. The data are used to monitor traffic (speed, direction, and size of vehicles) and to assess the quality of the roadway surface. The interpretation of dataset from traffic sources could then be used by engineers to improve and plan the efficient use of the transportation infrastructure.

The titles and details for each of the chapters follow:

- **Chapter 2: Particle velocity polarization for the evaluation of P and S-waves arrival for the PoroTomo Project in the Brady Hot Springs Geothermal Site**

  The purpose of this project to improve the determination P-wave time arrivals and extending the S-wave time arrivals by the polarization of particle motions as different wavefronts arrive at the nodal geophones deployed at Brady Hot Springs geothermal site. These results can be then be incorporated to velocity models to improve the high-resolution imaging of the geothermal site.

- **Chapter 3: Horizontal-to-Vertical Spectral Ratio to Estimate the Thickness of Sedimentary Deposits at the PoroTomo site in Brady Hot Springs, Nevada (USA)**

  The motivation for this study is the determination of the depth to the bedrock surface at Brady Hot Springs geothermal field with passive seismic response of the Nodal geophone array. The method requires the input of the S-wave velocity of the shallow sediments. We used two sets of S-wave velocity profiles: one discrete model based on ambient noise tomography and one continuous model based on the S-wave velocity increase with effective stress in unconsolidated sediments.

- **Chapter 4: Traffic Monitoring using Distributed Acoustic Sensing (DAS) at Garner Valley, California & Brady Hot Springs, Nevada**

  The goal of this chapter is to use seismic sources generated by highway traffic for the monitoring traffic patterns (e.g., number, directions, speeds, and size of travelling vehicles) and evaluating the quality of the roadway surface. The data collected and analysis performed on data from a high-density sensor array could help the Departments of Transportation in the monitoring of the use and the quality of the transportation infrastructure.

Chapter 2: Particle velocity polarization for the evaluation of P and S-waves arrival for the PoroTomo Project in the Brady Hot Springs Geothermal Site

2.1 Abstract

As part of the PoroTomo Project, active and passive seismic data were collected with a three-component seismometer array in order to image petrophysical properties of a 1500-m by 500-m by 400-m volume in a geothermal field at Brady Hot Springs, Nevada. We intended to use the arrival of multiple phases including P, S, and surface waves to invert for the distribution of petrophysical parameters, including Young's modulus, shear modulus, Poisson's ratio, density and porosity with an expected resolution of 50 m or better at a depth of 200 m. Since the determination of arrival times of S-waves is challenging, we implemented an analysis based on polarized particle motion to assess the arrivals of different phases. The methodology included rotation, filtering, cross-correlation, and stacking of waves generated by a vibroseis truck and captured by a the Nodal seismograph array. The determination of body and surface wave travel times were made by the changes in the obtained particle velocity polarization caused by the anisotropy and heterogeneity of the formation. In spite of these challenges, the obtained results provide a robust and tested methodology to determine arrival times of different phases. These arrival times could then be fed into neural network algorithm to provide a larger dataset and be used for overall inversion of P- and S-wave travel time tomographic images.

Keywords: Anisotropy; Body waves; Particle Motion; Polarization; Seismic; Surface waves

2.2 Introduction

Determining the arrival times of surface waves and body waves for seismic tomography studies is important in order to gather information about the distribution of poroelastic parameters in the study area. Body waves and surface waves have definite polarization patterns (Aki and Richards, 1980; Gal'perin, 1984), and these polarization patterns can then be used to assess the arrival times of different phases. While P-wave arrival times are relatively simple to determine, the S-wave arrival is much more difficult to assess as the S-wave arrivals are typically masked within the coda of P waves and surface waves. This paper presents a methodology to assess arrival times of P and S-waves using polarization analysis for the interpretation of seismic data obtained from Brady Hot Springs geothermal field in NW Nevada. The methodology was compared to an automated AIC picker used by Parker (2017) to capture the P-wave arrivals and then extended to determine S-wave arrival times.

2.3 The PoroTomo Project

The Poroelastic Tomography by Adjoint Inverse Modeling of Data from Seismology, Geodesy, and Hydrology Project (PoroTomo) is a technology demonstration project for the imaging of a geothermal field in Brady Hot Springs, Nevada (Figure 2.1). The project deployed different sensor arrays to both actively and passively collect seismic datasets, evaluate subsidence, and monitory hydrogeological process for the characterization of petrophysical parameters of in a volume of 1500 m by 500 m by 400 m overlying the geothermal field. This volume of study was named the PoroTomo Laboratory. The datasets include measuring the deformation of the Earth's surface using the Global Positioning System (GPS) and

Interferometric Synthetic Aperture Radar (InSAR), monitoring time series of hydraulic pressure and flow only indirectly in wells across the geothermal field, monitoring temperature histories both on the surface of the formation and in a borehole, and recording active and passive seismic waveforms using a Nodal seismometer array and surface and borehole distributed acoustic sensing (DASh and DASv) arrays. Figure 2.2 shows the map of the study area and the locations of the sensor arrays used during the PoroTomo project. The objective of the PoroTomo Project is the assessment of a combination of sensor technology to characterize and monitor changes in an enhanced geothermal system (EGS) reservoir (Feigl et al., 2017).

2.4 Geology of Brady Hot Springs

The Northern Great Basin in the western United States where Brady Hot Springs is located has many geothermal sites and activities controlled by active extensional tectonics (i.e., non-magmatic geothermal activities - Faulds et al., 2010). These geothermal sites were created as the result of high fluid and heat flow resulting from tectonic extensions. Brady Hot Springs is one of the three main geothermal fields in the Northern Hot Springs Mountains in Northwest Nevada (Figure 2.1). The area consists mainly of Miocene volcanic and sedimentary rocks. The area is cut by many NNE-striking faults (Figure 2.3 - Faulds et al. 2004). The Brady Hot Springs' geothermal field has been operated with 26 MWe power plant capacity since 1992 (Faulds et al., 2010). The reservoir temperature of the Brady geothermal field is 180-193°C at depths between 1 and 2 km (Benoit et al., 1982). At shallow depths, the Brady geothermal site is formed by independent thermal plumes (Benoit et al., 1982).

2.5 Data Acquisition and Methods

The PoroTomo Project gathered active and passive seismic data at the Brady Hot Springs Geothermal Natural Laboratory with two types of sensor arrays: Nodal Geophone Array (Parker et al. 2018) and Distributed Acoustic Sensing (DAS) array (Wang et al. 2018). During the testing period, there were four three-day stages of injection and production of the geothermal plant. While the first stage was set at normal levels of production, the second stage included no production with limited extraction or injection of fluid into the geothermal reservoir. The third stage included a period of high injection and pulses of increase injection pressure. During the last stage, pumping was returned to normal production (Parker, 2017).

During these different production stages, the research team deployed a source of seismic waves, a large vibroseis truck (T-Rex – University of Texas-Austin), at 196 locations (Figure 2.4). The vibroseis truck generated seismic waves into the PoroTomo Laboratory in three vibration modes: vertical, longitudinal, and transversal to the main axis of the vibroseis truck. These vibrations modes were repeated three times in each location. The Vibroseis truck was aligned in the NNE direction (parallel to the Interstate highway I-80 - Figure 2.4). A total of 6633 vibroseis events were recorded. A swept-frequency signal was generated between 5 and 80 Hz during a 20 seconds period (Parker et al., 2018). The generated signal was captured with two arrays: an 8700-m horizontal and 400-m vertical DAS array (Feigl et al. 2017; Wang et al. 2018) and a 238 Nodal 3-component seismograph array (Feigl et al. 2017). The Nodal seismograph array was deployed over a 1.6 km by 1.3 km area to map the response of a central volume of 1.6 km long by 0.5 km wide by 0.4 km deep (Figure 2.2). The Nodal seismographs were spaced approximately 60 m apart in the inner volume of interest and 200 m apart in the section outside

the PoroTomo Laboratory. For 16 days data were captured with the 238 3D-component Nodal geophones (Parker, 2017).

The collected seismic data were then cross-correlated with the vibroseis sweep signals to determine P-wave arrivals using an automated AIC picker (Parker et al., 2018). The sets of P-wave arrivals were then used to invert for tomographic images of the PoroTomo Laboratory (Parker et al., 2018). However, the methodology used by Parker (2017) was not able to determine S-wave arrivals. The objective of this study is to propose and test an alternative methodology to improve P-wave arrival determination and to expand it to determine S-wave arrivals.

2.6 Polarization of Particle Motion

Since the automated AIC-picker used by Parker et al. (2018) could not reliably pick S-wave arrival times, we proposed a polarization method that analyzes particle motions of the active seismic data to determine the arrival of both P- and S-wave phases. Figure 2.5 describes the particle motions of P, SV, and SH waves propagating through a homogenous-isotropic medium, a heterogeneous-isotropic medium, and homogenous-anisotropic medium. As seen in Figure 2.5a, the particle motion of P, SH, and SV waves in homogenous-isotropic media corresponds to the polarization direction as defined for each wave: parallel to the direction of waves propagation for the P-wave, vertically perpendicular to the wave propagation direction for the SV-wave, and the horizontally perpendicular to the wave propagation direction for the SH-wave. On the other hand, Figure 2.5b shows that the P-, SH-, and SV-wave particle motions change for heterogeneous-isotropic media and are dependent on the reflection angle. That is, the

particle motions in heterogeneous-isotropic medium are the same as the particle motion in homogenous-isotropic media even though the polarization direction of the waves on the vertical vs radial and transversal vs radial planes. The direction of particle motion depends on the direction of incidence of the different waves. The P-, SH-, and SV-wave particle motions in homogenous-anisotropic media become increasingly complex: the polarization planes become crossed like an x and/or rotated as shown in Figure 2.5c. The interpretation of the polarized arrival is the basis for the proposed interpretation methodology. That is, the polarization of the particle motion changes change in an anisotropic media as perturbed, rotated, crossed, and/or complicated polarized shapes (Crampin, 1975). Anisotropic zones may affect seismic waves in various ways. The anomalies can be observed in the travel times of the waves, the seismic velocities of the waves, surface wave dispersion, body wave amplitudes, and the relationship between P, SH, and, SV waves. However, isotropic structures do not cause these anomalies, which help us to make suggestions about whether a study area includes isotropic or anisotropic formations (Crampin, 1975). Furthermore, Rayleigh waves in an isotropic medium will show a retrograde elliptical particle motion with the main axis in the vertical direction. In an anisotropic medium, the main axis of the particle motion ellipse will tilt forward. Crampin (1975) asserted that an *Inclined Rayleigh wave* coupled with or without Love wave implies anisotropic structures. When we tried to determined Love wave arrival times, we realized that they imply that they were observed coupled with Rayleigh waves and/or indicated an angle to Rayleigh wave up to 90°. Crampin (1966a, 1967) noticed coupling due to the presence of anisotropic zones within a geological formation.

2.7 Processing of the Data

The collected seismic data were pre-processed for interpretation. These pre-processing steps were necessary because the direction of the vibroseis truck and the orientation of the Nodal geophones did not coincide. Aligning the responses to a common set of directions facilitates the interpretation of the particle motion to assess the arrival of P- and S-waves. For this study the directions of analysis were select to be in the vertical direction, in the radial direction (parallel to the direction of vibroseis-Nodal direction), and transverse direction (perpendicular to the direction of vibroseis-Nodal direction).

The following set of steps was implemented: *rotation* of the particle motion responses, *filtering* of the recorded signals, *cross-correlation* of the collected data with the input signal from the vibroseis, *staking* of multiple signals to improve signal-to-noise ratio, and *interpretation* of polarization data. A detailed description of the implementation of these steps follows.

1. *The rotation* was the first step of the data processing. The vibroseis truck created the waves by vibrating in three directions (Figure 2.4): vertical, horizontal parallel to the main axis of the vibroseis truck, and horizontal perpendicular to the main axis of the Vibroseis truck. However, the Nodal geophones were not aligned in the same direction as the vibroseis truck except for the vertical direction (the x-axis of the Nodal seismograph was oriented in the NS direction). Therefore, a rotation of the horizontal components of the Nodal responses was required to align them into a consistent coordinate systems: radial and transversal directions with respect the vibroseis-Nodal direction (Figure 2.4). The modified equations for the PoroTomo seismic data below were used to rotate from inline-crossline (x, y) coordinates to radial-transversal (r, t) coordinates with respect to the direction of wave propagation (Figure 2.4).

$$\text{Radial} = -\text{NNW} \cdot \cos(\varphi) - \text{ENE} \cdot \sin(\varphi) \quad (2.1)$$

$$\text{Transversal} = \text{NNW} \cdot \sin(\varphi) - \text{ENE} \cdot \cos(\varphi) \quad (2.2)$$

In these equations, ENE and NNW represent the horizontal component records created by the source in ENE and NNW directions, respectively. φ represents the angle between the directions of the horizontal components of Nodal and the directions of the truck components shown in Figure 2.4.

2. *A bandpass filter* was applied from 5 to 80 Hz. The vibroseis created swept signals between 5 and 80 Hz. However, two roads (Interstate I-80 and a service road) next to the study area created uncorrelated waves with different frequencies. That is why a band-pass filter between 5 - 80 Hz was applied to the data to improve the signal-to-noise ratio of the collected datasets (Parker, 2017).

3. The *Cross-correlation* function provides a way to remove the vibroseis sweep and produce an estimate of the Green's function response since the Nodal responses include an embedded sweep. After the cross-correlation operation, the traces theoretically include only information about the geology of the study area. This means that the cross-correlation operation is a method similar to filtering to remove unwanted frequencies and uncorrelated signatures (Brittle et al., 2001). Brittle et al. (2001) expressed the connection between the recorded trace and the vibroseis source with the following equation:

$$x(t) = r(t) * s(t), \quad (2.3)$$

where x(t) is the recorded data, s(t) is the source sweep, r(t) is only for reflection geology, and * is the convolution operator. Cross-correlation ($\otimes$) is applied on the trace and the sweep to remove the sweep. To cross-correlate the sweep, the equation is

$$x_{CC}(t) = r(t) * s(t) \otimes s(t). \quad (2.4)$$

The simplified equation for the cross-correlated sweep is

$$x_{CC}(t) = r(t) * k(t), \quad (2.5)$$

where Klauder's wavelet, $k(t)$, is the definition of the cross-correlated sweep signal.

Although deconvolution and cross-correlation functions are both common methods to remove the sweeps from the recorded traces (Brittle et al., 2001), the cross-correlation function is preferred for this study because the deconvolution function was unable to remove high-frequency noise from the traces (Parker et al., 2018). Moreover, even though cross-correlation and deconvolution functions had similar results, the cross-correlation functions yields slightly higher signal-to-noise ratio (Parker et al., 2018).

4. *Stacking* was applied after the cross-correlation operation. With stacking the cross-correlated traces, the waveforms are enhanced because the stacked waveforms include all instances of a sweep mode of one vibepoint and reduce the effect of uncorrelated signatures (Santamarina and Fratta, 2005).

5. The *Polarization method* is used to help identify the time arrivals of different phases. The method guides the picking of arrival times by monitoring changes in the particle motions in two polarization planes (i.e., radial vs. vertical and radial vs. transversal polarization planes). The automated picker presented by Parker et al. (2018) worked well for evaluating the P-wave arrivals for most of the Nodal geophones but it was not able to determine the arrival of S-waves (Parker 2017). Parker (2017)'s picking algorithm occasionally picked random S-wave arrival times. For this reason, the polarization

method was validated with Parker's P-wave time arrivals and was extended for the determination S-wave time arrivals.

Body waves in the sagittal plane (P and SV motion) can be combined with waves in the transverse plane to help evaluate phase arrivals in anisotropic propagation media (SH motion - Keith and Crampin, 1977). In addition, Rayleigh wave particle motion is going to be observed as *Inclined Rayleigh wave* as a sign of anisotropic structures and/or the Rayleigh wave and Love wave may arrive in seismograms together/mixed with each other (Crampin, 1975).

2.8 Results and Discussion

As a result of the data processing, the particle motion seems to indicate the presence of anisotropic structures because of the perturbed, crossed, and/or complicated shape of the particle motion of the wave arrivals. Each type of wave for each trace indicates some anisotropic anomalies based on their particle motions. Figure 2.6 shows the estimated arrival times for two Nodal record results. P-wave and S-wave predicted arrival times indicate that the P- wave and S-wave particle motion is in an isotropic media like the expected response presented in Figure 2.5. Keith and Crampin (1977) concluded that anisotropic structures/zones may result in variations in the refraction and critical angles. They also indicated that anisotropy creates changes in the polarization of the different phases causing cross-coupling between P-, SH-, and SV- incident, reflected and refracted waves since the particle motion of the waves are affected by anisotropy but the polarity of the incident wave is not.

The polarization method was used for the determination of P- and S-wave phase arrivals where auto-pickers did not give satisfactory results. Since the coordinates of the Nodals were not

aligned with the coordinates the vibroseis truck, radial and transverse directions were obtained by rotation of the coordinates. One challenge in the interpretation of the processed data is caused by the heterogeneity and anisotropy in the near-surface geology. Anisotropy produces body waves with no pure P, SV, or SH particle motions: waves in the vertical plane - P and SV motions – might show transverse motions. Anisotropy results in S-waves that are separated as more complicated SV and SH components (Keith and Crampin, 1977).The character of the particle motions can be assessed as perturbed and complicated due to anisotropy.

Polarization plots in Figure 2.7 were obtained as the result of processing. The presented results are from two pairs of source/Nodal sensor. The only difference between the figures is that they were gathered for different modes of excitation: vertical, longitudinal, and transverse. The shape of the particle motion of the waves implies anisotropic structures. While the polarization method worked for some of the data to determine the arrival times, it did not capture all the phases in the vibroseis events.

We compared our results with the arrival times obtained with AIC-pickers (Sleeman and van Eck, 1999), energy methods, and automated AIC-picker (Parker et al., 2018) in Figures 2.7 and 2.8. The AIC-picker results were obtained with the following formula:

$$AIC(k,1) = k \cdot log(var1) + (N - k - 1) \cdot log(var2) \tag{2.6}$$

which evaluates the statistics of a whole signal after k-th position and before k-th time position within the signal. For the automated AIC picker, we used the results obtained by Parker et al. (2018) who used AIC-picker combined with STA/LTA for the distances not more than 150 m. Lastly, energy picking methodology were obtained to determine P- and S-wave travel time with the following formula:

$$Energy = u_{radial}^2 + u_{transversal}^2 + u_{vertical}^2 \quad (2.7)$$

where u_{radial}, $u_{transversal}$, and $u_{vertical}$ are the three-component recorded and processed waves of the Nodals. For energy picking method, we expect P-wave travel times as the first energy in receivers and S-wave travel times as the first high energy in receivers.

The travel time for P-waves and S-waves captured is the polarization method very similar to the travel times captured from AIC-picker and energy picking methods. However, the travel time for P-waves from the automated AIC-picker method tends to yield earlier times compared to the polarization method in the radial mode of vibration. Also, the vertical mode of vibration provides a better estimate of the P-wave travel times as compared to the radial and transversal vibration mode (Figure 2.8). While determining S-wave travel times appear more consistent for longitudinal mode of vibration as compared to vertical and transversal modes of vibration. We were not able to consistently determine P-wave travel times higher than 0.6 seconds and S-wave travel times higher than 1.2 seconds (Figure 2.8). The reason for that is that as the distance between vibroseis truck and the Nodal geophone increases, the signal-to-noise ratio of the captured traces decreases. Due the dispersion nature of surface waves, we could not determine the Rayleigh and Love wave arrival times for the most Nodal responses in the PoroTomo Laboratory in Brady Hot Springs.

2.9 Conclusions

This study presents a methodology for the particle motion analysis of P and S-waves to determine their arrival times for the PoroTomo project site. The PoroTomo Team collected the seismic data at Brady Hot Springs, Nevada. Three component seismogram data recorded by the

PoroTomo Team was subjected to preprocessing: rotation, filtering, cross-correlation, stacking, and polarization. The results of this study imply that there are anisotropic structures in the study area. Even though P-wave arrivals were easily determined with a set of auto-pickers by Parker et al. (2018), this did not work well for the determination of S-wave arrivals and later phase time arrivals. Polarization interpretation of traces can be successfully used to evaluate the arrivals of multiple phases on the data from Brady Hot Springs. The determination of S-wave and later phase time arrivals in a limited number of traces can in future be input in neural network algorithms to expand the analysis to the whole survey campaign at Brady Hot Springs.

2.10 Acknowledgments

The work presented herein was funded in part by the Office of Energy Efficiency and Renewable Energy (EERE), U.S. Department of Energy, under Award Number DE-EE0006760, and by the General Directorate of Mineral Research and Exploration and the General Directorate of Higher and International Education (The Republic of Turkey). The authors appreciate the PoroTomo Team for their support.

2.11 References

Aki, K. and P. G. Richards (1980). Quantitative Seismology, Theory and Methods, W. H. Freeman and Co., San Francisco, California, 768 pp.

Benoit, D. A., Puglisi, F. A., and Olson, D. L. (1982). A fathead minnow Pimephales promelas early life stage toxicity test method evaluation and exposure to four organic chemicals. Environmental Pollution Series A, Ecological and Biological, 28(3), 189-197.

Brittle, K. F., Lines, L. R., and Dey, A. K. (2001). Vibroseis deconvolution: a comparison of cross-correlation and frequency-domain sweep deconvolution. Geophysical Prospecting, 49(6), 675-686.

Crampin, S. (1966a). Higher modes of seismic surface waves: propagation in Eurasia. *Bulletin of the Seismological Society of America*, *56*(6), 1227-1239.

Crampin, S. (1967). Coupled Rayleigh-Love second modes. Geophysical Journal International, 12(3), 229-235.

Crampin, S. (1975). Distinctive particle motion of surface waves as a diagnostic of anisotropic layering. *Geophysical Journal International*, *40*(2), 177-186.

Crampin, S. and King, D. W. (1977). Evidence for anisotropy in the upper mantle beneath Eurasia from the polarization of higher mode seismic surface waves. *Geophysical Journal of the Royal Astronomical Society*, 49(1), 59-85.

Faulds, J. E., Coolbaugh, M. F., Benoit, D., Oppliger, G., Perkins, M., Moeck, I., and Drakos, P. (2010). Structural Controls of Geothermal Activity in the Northern Hot Springs Mountains, Western Nevada: The Tale of Three Geothermal Systems (Brady's, Desert Peak, and Desert Queen), Geothermal Resources Council Transactions, 34, 675-683.

Faulds, J. E., Coolbaugh, M. F., Vice, G. S., and Edwards, M. L. (2006), Characterizing Structural Controls of Geothermal Fields in the Northwestern Great Basin: A Progress Report, Geothermal Resources Council Transactions, 30, 69-76.

Faulds, J. E. (2011), Assessment of favorable structural settings of geothermal systems in the great basin region, western USA, paper presented at 2011 GSA Annual Meeting in Minneapolis.

Faulds, J., Moeck, I., Drakos, P., and Zemach, E. (2004). Structural assessment and 3D geological modeling of the Brady's geothermal area, Churchill county (Nevada, USA): A preliminary report, paper presented at Thirty-Fifth Workshop on Geothermal Reservoir Engineering, Stanford University, Stanford, California.

Feigl, K. L., and the PoroTomo Team (2017). Overview and preliminary results from the PoroTomo project at Brady Hot Springs, Nevada: poroelastic tomography by adjoint inverse modeling of data from seismology, geodesy, and hydrology. In 42nd Stanford Workshop on Geothermal Reservoir Engineering (p. 15). Stanford, CA: Stanford University.

Gal'perin, E. I. (1984). The Polarization Method of Seismic Exploration, Reidel Publishing Co., Boston, Massachusetts.

Gaiser, J. E. (1999). Applications for vector coordinate systems of 3-D converted-wave data. The Leading Edge, 18(11), 1290-1300.

Jolie, E., Moeck, I. and Faulds, J. E. (2015). Quantitative structural–geological exploration of fault-controlled geothermal systems—A case study from the Basin-and-Range Province, Nevada (USA), Geothermics, 54, 54-67.

Keith, C. M. and Crampin, S. (1977). Seismic body waves in anisotropic media: reflection and refraction at a plane interface. Geophysical Journal International, 49(1), 181-208.

Parker, L. M. (2017). Active Source 3d Seismic Tomography of Brady Hot Springs Geothermal Field, Nevada (Master's Thesis, University of Wisconsin – Madison, USA).

Parker, L. M., Thurber, C. H., Zeng, X., Li, P., Lord, N. E., Fratta, D., Wang, H.F., Robertson, M.C., Thomas, A.M., Karplus, M.S. and Nayak, A. (2018). Active-source seismic tomography at the Brady Geothermal Field, Nevada, with dense Nodal and fiber-optic seismic arrays. Seismological Research Letters, 89(5), 1629-1640.

Santamarina, J. C. and Fratta, D. (2005). Discrete signals and inverse problems: an introduction for engineers and scientists. John Wiley & Sons.

Santamarina, J. C., Klein, K. A., and Fam, M. A. (2011). Soils and Waves. John Wiley and Sons.

Shevenell, L., G. Oppliger, M. Coolbaugh, and J. Faulds (2012). Bradys (Nevada) InSAR Anomaly Evaluated with Historical Well Temperature and Pressure Data, Geothermal Resources Council Transactions, 36, 1383-1390.

Sleeman R. and van Eck, T. (1999). Robust automatic P-phase picking: An on-line implementation in the analysis of broadband seismogram recordings, Phys. Earth Planet. Int., 113, 265–275.

Wang, H. F., Zeng, X., Miller, D. E., Fratta, D., Feigl, K. L., Thurber, C. H., and Mellors, R. J. (2018). Ground motion response to an ML 4.3 earthquake using co-located distributed acoustic sensing and seismometer arrays. Geophysical Journal International, 213(3), 2020-2036.

Figures

Figure 2.1 *Map of the study area. Brady Hot Springs geothermal field is located in Northwest Nevada (Map: Google Earth).*

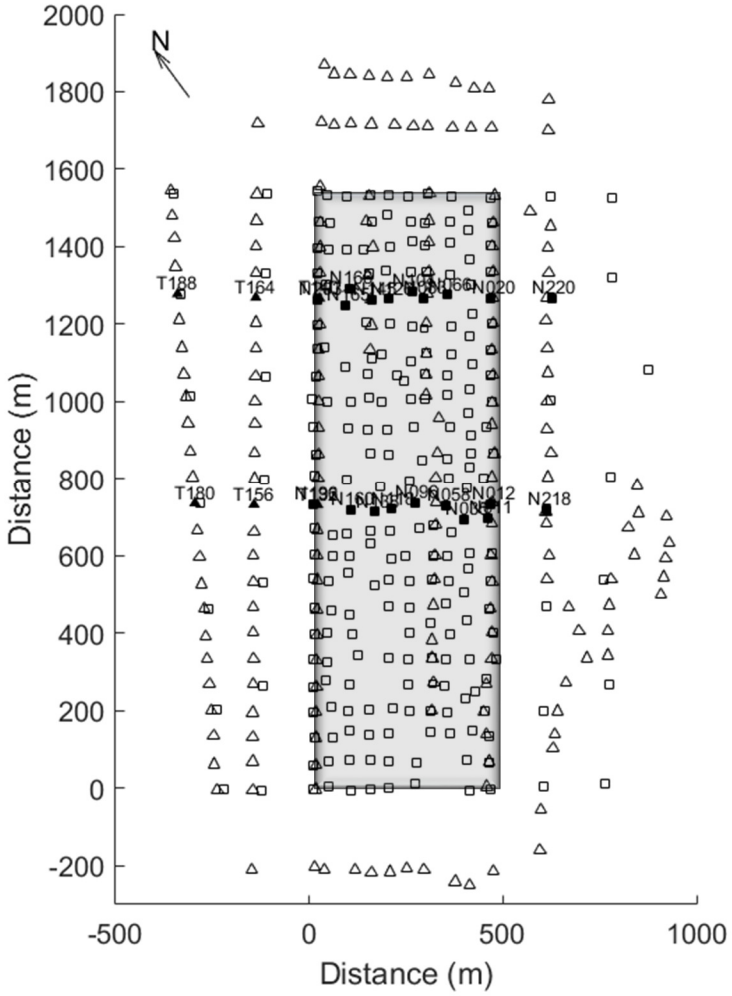

Figure 2.2 *Map of the study area. Map of study area shows volume targeted for seismic tomography (gray shading), vibroseis points of manually determined P- and S-wave arrival times (black filled triangles, labeled T), Nodal seismometers of manually determined P- and S-wave arrival times (black filled squares, labeled N), vibroseis points (black empty triangles), and Nodal seismometers (black empty squares).*

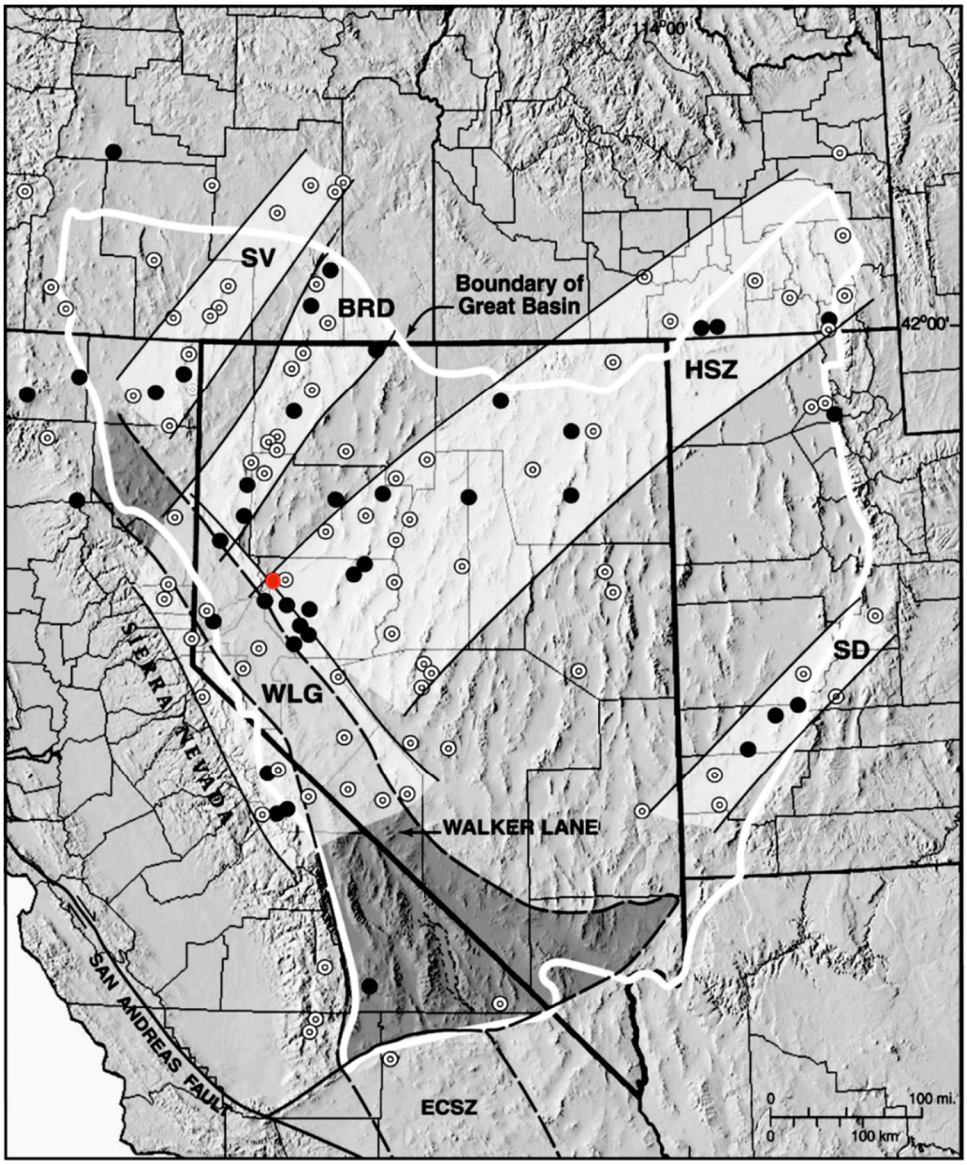

Figure 2.3 The map of the Great Basin in North Western United States. The red dot shows the location of the Brady Hot Springs (Faulds et al. 2004).

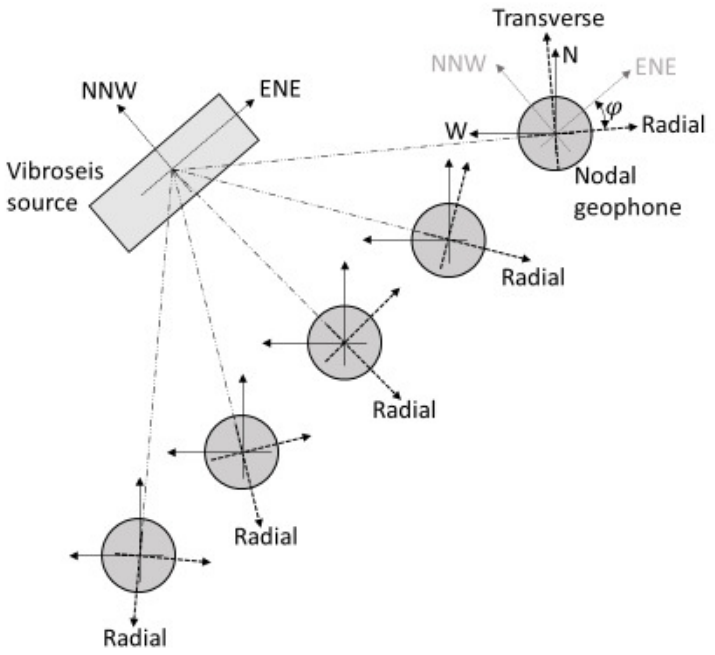

Figure 2.4 *Acquisition coordinate system for the data gathered by PoroTomo Team. Since the directions of the seismic waves were not recorded in the desired direction, a common direction for each geophone (radial and transverse) was obtained with rotation technique. The rotation technique on the seismic records followed the procedure described by Gaiser (1999).*

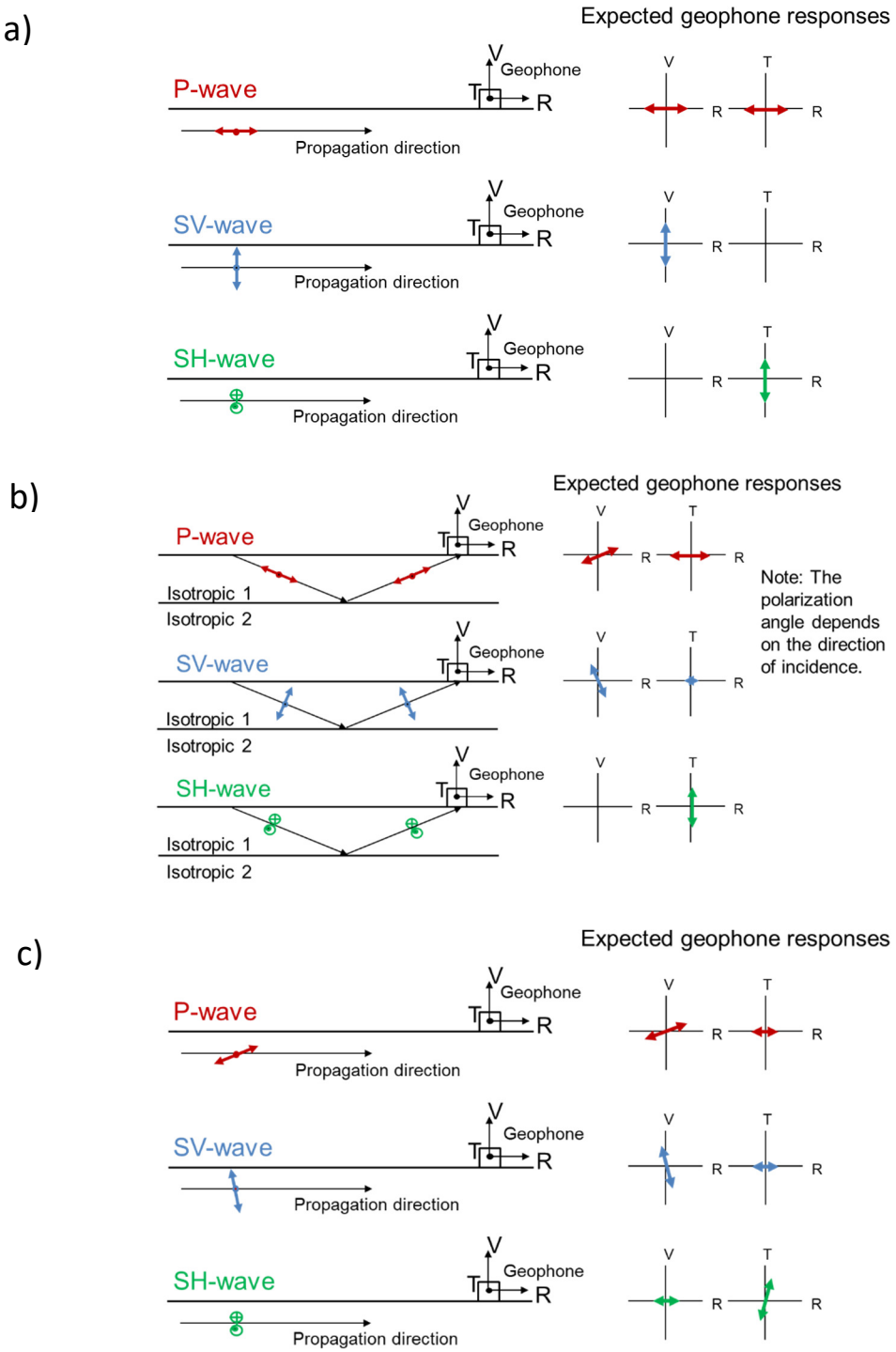

Figure 2.5 Particle motion of P, SH, and SV waves through (a) homogeneous-isotropic, (b) heterogeneous-isotropic and (c) anisotropic-homogenous structures. Particle motion for P- and S-waves in homogenous-isotropic and heterogeneous-isotropic are in the same direction and perpendicular to wave propagation direction, respectively. We see them in the geophone like shown in the figures. For anisotropic structures, the particle motion is going to change as both shape and direction.

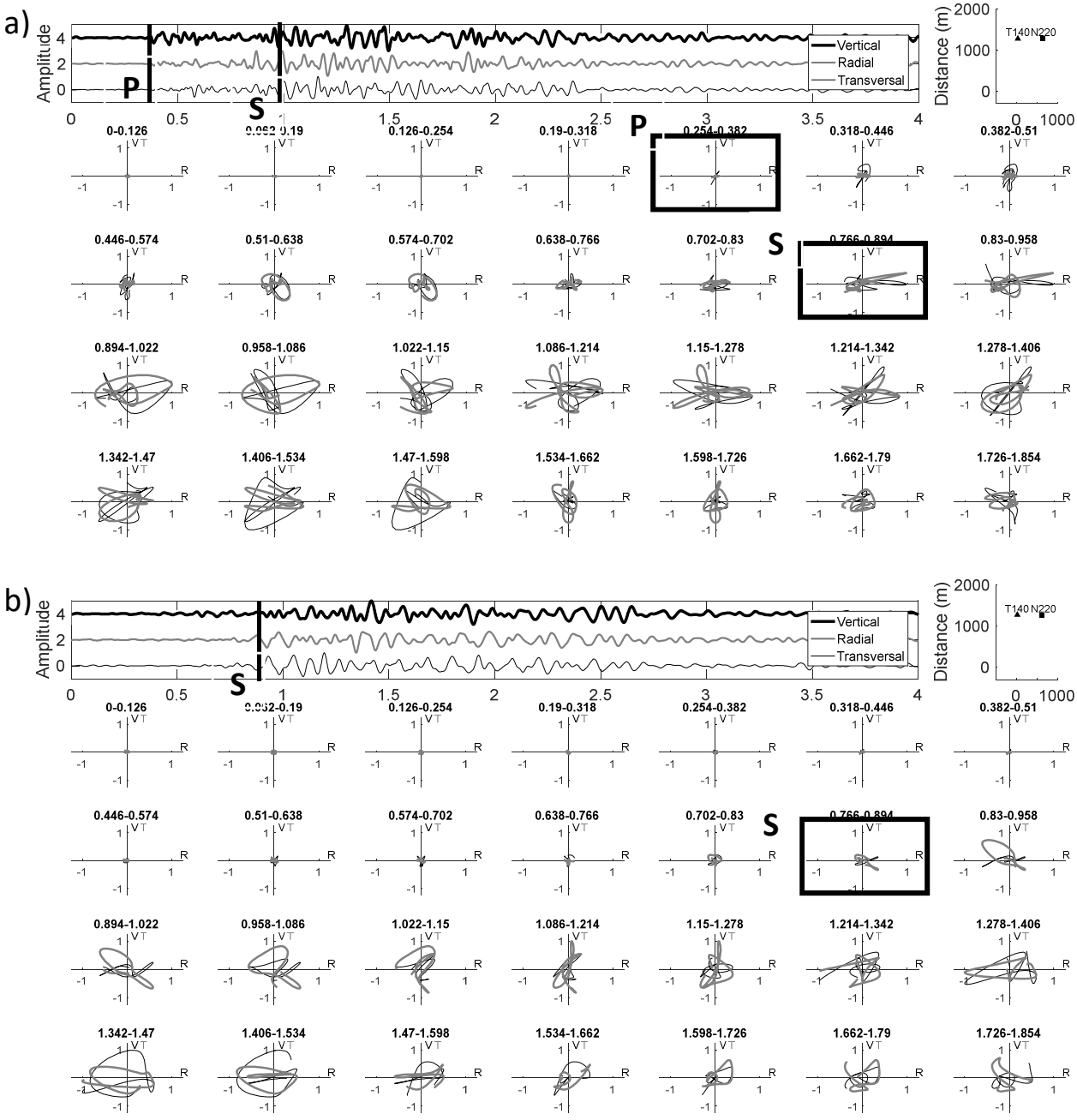
a)
Amplitude
Vertical
Radial
Transversal
P
S
Distance (m)
T140 N220
0-0.126
0.126-0.254
0.19-0.318
0.254-0.382
0.318-0.446
0.382-0.51
0.446-0.574
0.51-0.638
0.574-0.702
0.638-0.766
0.702-0.83
0.766-0.894
0.83-0.958
0.894-1.022
0.958-1.086
1.022-1.15
1.086-1.214
1.15-1.278
1.214-1.342
1.278-1.406
1.342-1.47
1.406-1.534
1.47-1.598
1.534-1.662
1.598-1.726
1.662-1.79
1.726-1.854
b)
Amplitude
Vertical
Radial
Transversal
S
Distance (m)
T140 N220

c)

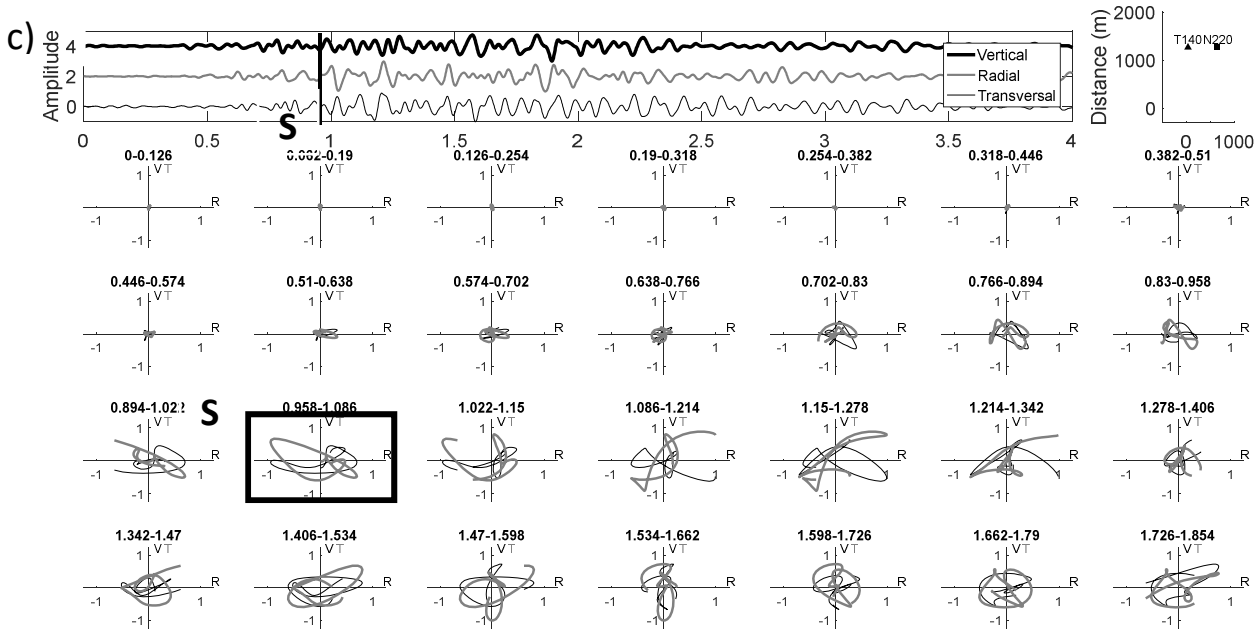

Figure 2.6 *Particle motion observations for (a) vertical, (b) longitudinal, and (c) transversal mode of vibroseis mode. The inset map on the top right shows the Nodal and vibroseis locations symbolized with square and triangle, respectively. The traces on the top left of each of the panes correspond to the vertical, radial, and transversal direction traces of the Nodal responses. The time windows with the rectangle indicate the time for (a) show predicted P-wave and S-wave arrival time, and time windows in the rectangle for (b) and (c) show the estimated S-wave arrival time.*

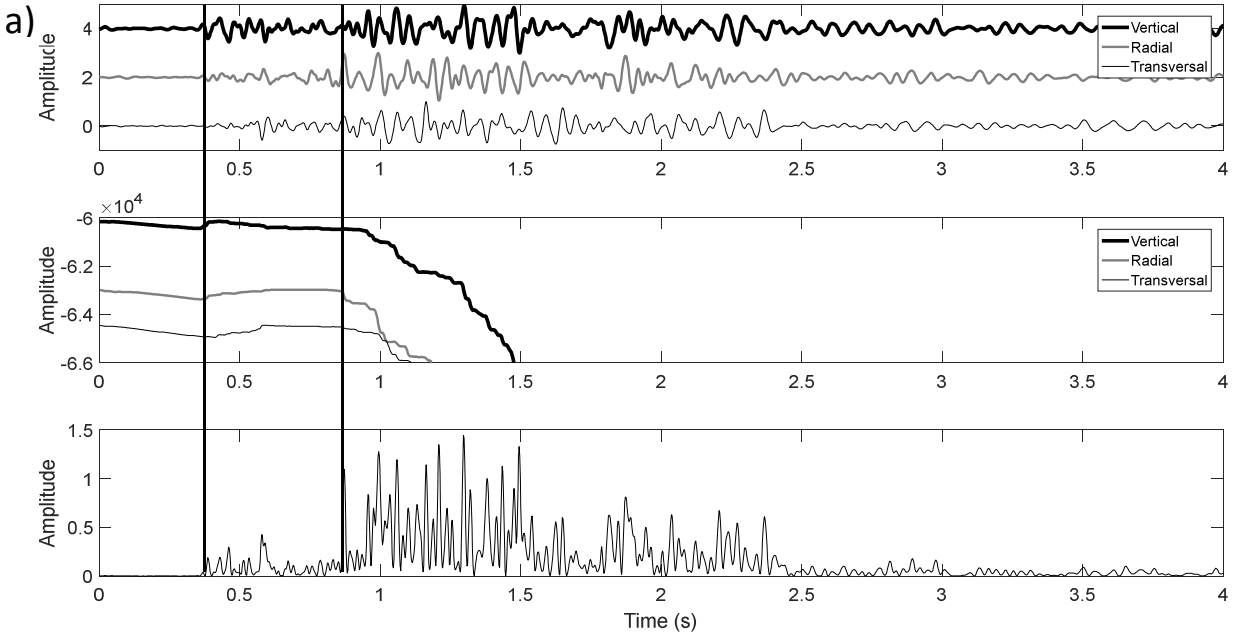
a)
Amplitude
Vertical
Radial
Transversal
×10^4
Time (s)

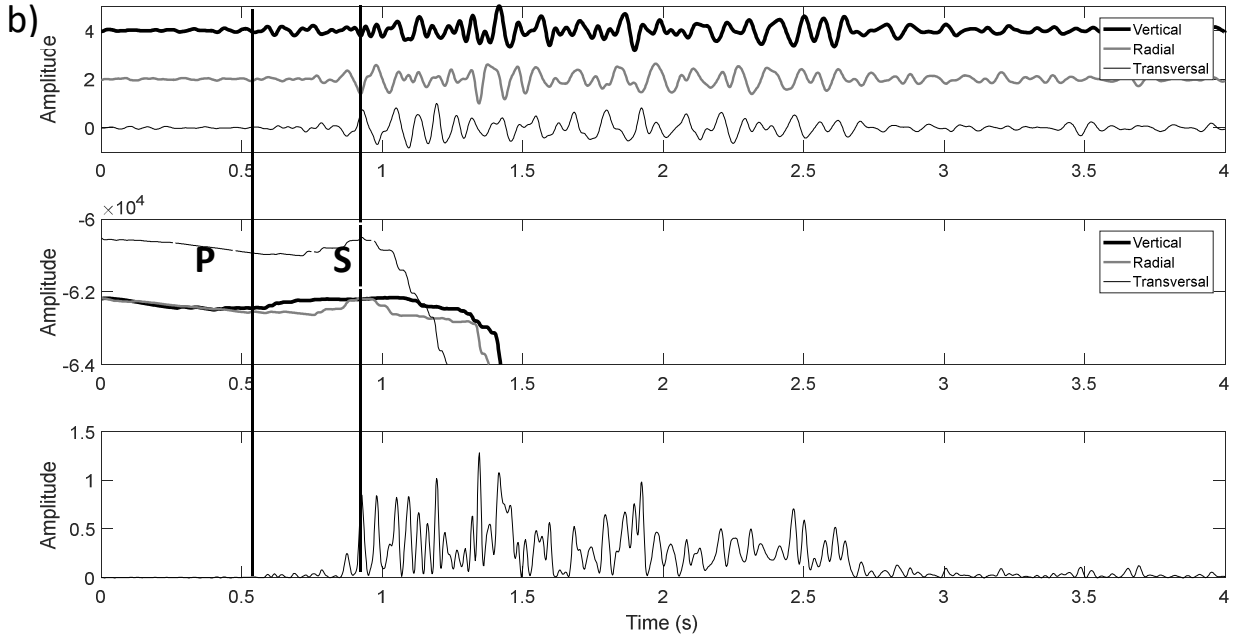
b)
Amplitude
Vertical
Radial
Transversal
×10^4
P
S
Time (s)

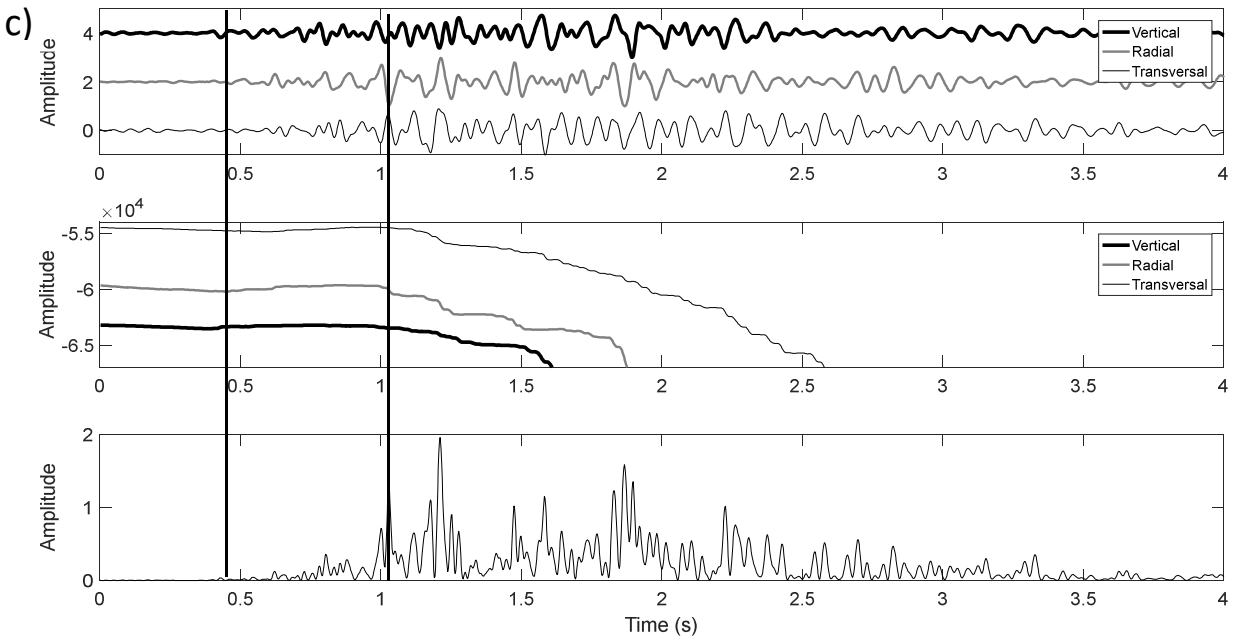

Figure 2.7 *Each graph in (a), (b), and (c) shows (a) stacked data, (b) AIC-pickers results, and (b) particle motion energy for vertical, longitudinal, and transversal components for the modes of vibroseis vibration.*

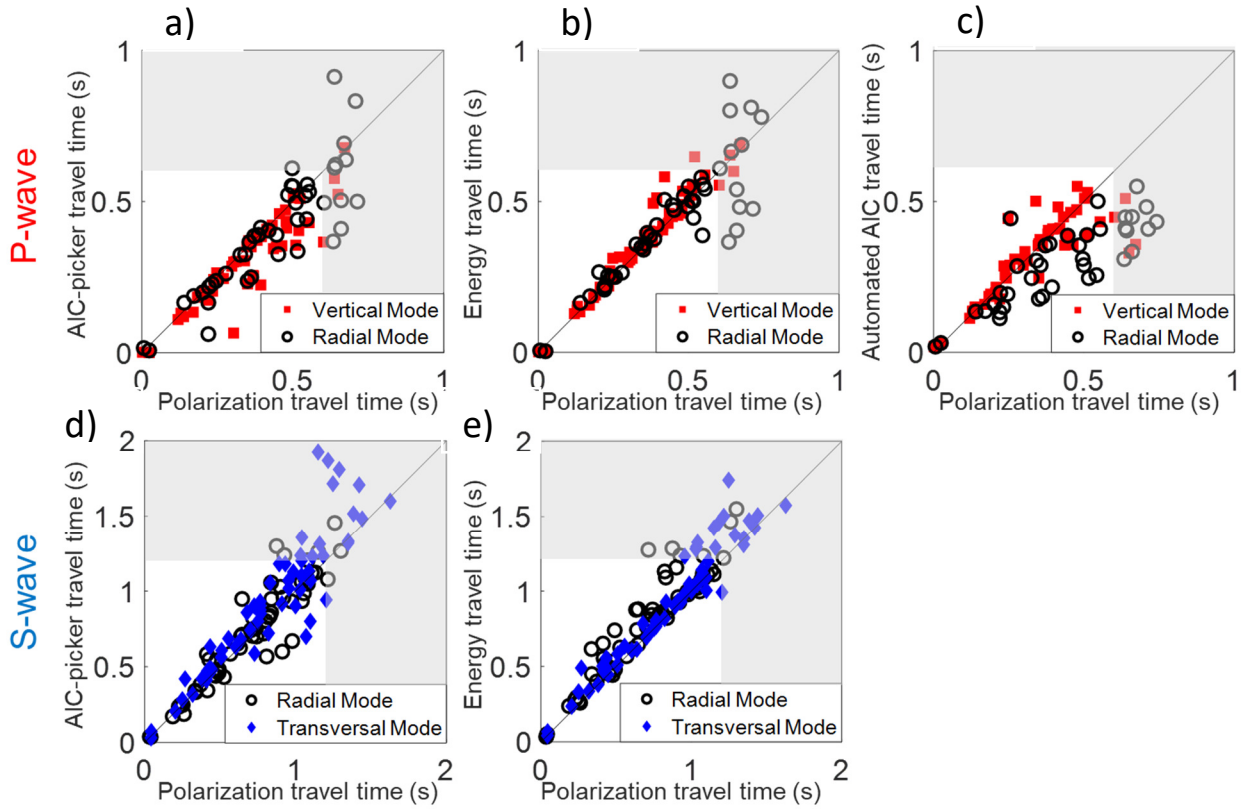

Figure 2.8 *The comparison of P- and S-waves arrival times between polarization method versus AIC-pickers and polarization method versus AIC-pickers. The graphics show polarization method versus AIC-pickers for P-wave in vertical vibration mode and radial vibration mode, polarization method versus energy for P-wave in vertical vibration mode and radial vibration mode, polarization method versus automated AIC-pickers for P-wave in vertical vibration mode and radial vibration mode, polarization method versus AIC-pickers for S-wave in radial vibration mode and transversal vibration mode, and polarization method versus energy for S-wave in radial vibration mode and transversal vibration mode for (a), (b), (c), (d), and (e), respectively.*

Chapter 3: Horizontal-to-Vertical Spectral Ratio to Estimate the Thickness of Sedimentary Deposits at the PoroTomo site in Brady Hot Springs, Nevada (USA)

3.1 Abstract

During March 2016, the PoroTomo research team deployed more than 8700 m of distributed acoustic sending (DAS) and distributed temperature (DTS) fiber optic cable in horizontal and vertical sensing arrays, 244 three-component surface Nodal geophones, obtained InSAR images, pressure transducers, and a vibroseis truck to actively and passively image the response of a geothermal field in Brady Hot Springs, Nevada. During the imaging period, the geothermal field was manipulated to change the pore pressure in the formation. The objective of the study was to invert for poroelastic parameters within a 1500 m by 500 m by 400 m volume using tomographic techniques. Among the different imaging techniques, the research team used passive horizontal-to-vertical spectral ratio (HVSR) data captured with the three-component Nodal geophones to estimate the thickness of the sedimentary deposits across the PoroTomo site. The interpretation of the inverted data is complicated due to the heterogeneity in the near-surface deposits at the site. These deposits include diatomaceous earth, sandy/silty layers, and hardened silica associated with the presence of fumaroles. In spite of the challenges associated with deposits of very different stiffness, the use of HVSR for mapping sediment thickness across the Natural Laboratory would help constrain the inversion models in an attempt to improve the quality of the solution images.

Keywords: HSVR, surface waves, ambient noise, seismology

3.2 Introduction

The PoroTomo Project team deployed Nodal geophones to record ambient noise. The purpose of this study is to estimate the thickness of the sedimentary deposits throughout the PoroTomo site by using the Nakamura (1989)'s method. The horizontal-to-vertical spectral ratios (HVSR) was a method proposed by Nakamura (1989) to assess the depth of sedimentary deposits over rigid bedrock layers. The method uses the microtremor method to gather ambient noise data and assess the depth of the layer by analyzing the dynamic response of the sediments. The method is useful for seismic microzonation studies (Herak, 2008).

3.3 The PoroTomo Project

The Poroelastic Tomography by Adjoint Inverse Modeling of Data from Seismology, Geodesy, and Hydrology Project (Porotomo) is a technology demonstration project to image the geophysical properties of a geothermal field in Brady Hot Springs, Nevada. Brady Hot Springs is a geothermal field in the Northern Great Basin in the western United States. The Brady Hot Springs is not magmatic controlled but is tectonically controlled formation (Faulds et al., 2010). The Hot Springs Mountains including Brady Hot Springs are mostly constituted of sedimentary rocks (Faulds et al., 2010). For example, several wells at Brady Hot Springs show the presence of late Oligocene ash-flow tuffs while late Miocene to Quaternary basin-fill sediments primarily are observed in the western part of the Brady Hot Springs field (Faulds et al., 2010).

During the study, the Porotomo team used both active (vibroseis) and passive (ambient and traffic noise) sources to excite a 3-component Nodal geophone array and a horizontal and a vertical Distributed Acoustic Sensing (DASh and DASv) array to collect seismic wave datasets

for the characterization of petrophysical parameters of the study area. These petrophysical parameters included saturation, porosity, Young's modulus, Poisson's ratio, and density. The Porotomo Team also monitored deformation of the ground surface by using Global Positioning System (GPS) and Interferometric Synthetic Aperture Radar (InSAR). Finally, time series of hydraulic pressure and flow in wells across the geothermal field, distributed monitoring of temperature both on the surface of the formation and in a borehole, completed the sensing system. The map of the study area and the locations of the sensor arrays used during the PoroTomo project are shown in Figure 3.1. The goal of the PoroTomo Project is assessing a combination of sensor technology to characterize and monitor changes in an enhanced geothermal system (EGS) reservoir (Feigl et al., 2017).

3.4 Data Acquisition Methodology

The PoroTomo Project at the Brady Hot Springs Geothermal Natural Laboratory obtained seismic data during four stages of injection and production of the geothermal plant: Stage 1 - normal levels of production, Stage 2- no production (shutdown) with limited extraction or injection of fluids into the geothermal reservoir, Stage 3- high injection and pulses of increased injection pressure, and Stage 4 - returning to normal production.

Of all the data available at the site, we used passive seismic data collected with 238 3-component Nodal geophones (Figure 3.1). These geophones have 5 Hz corner frequency and include a 24-bit digitizer. Their dynamic range is 127 dB. The data were sampled with 0.002-second sampling interval and ±10 μs using GPS timing. We analyzed the data from 00:00 – 01:00 am from day 23 (Stage 4 – after going back to normal production). These data were

analyzed to calculate the HVSR profiles and determine the peak in the frequency response. The frequency of the peak HVSR response is then used to calculate the depth of the sediment deposits. Four conditions were assessed on the HVSR responses: effect of Ormat Plant, the effect of I-80 traffic noise, the effect of pump operations during testing, and evaluation of data for the determination of sediment layer thickness.

3.5 Horizontal to Vertical Spectral Ratio

The HVSR is a method developed by Nakamura (1989) to assess the depth of sedimentary deposits over rigid bedrock. The method basically uses microtremors to gather data on the dynamic response of shallow deposits. The method is useful for seismic microzonation studies (Herak, 2008). Mucciarelli and Gallipoli (2001) raised concerns about the HVSR method, including the problem that there is no standard for data gathering/processing and there is no clear theoretical background for the interpretation. In spite of these issues, the HVSR method has been successful for microzonation studies by many researchers (including Motazedian et al., 2011; Mihaylov et al., 2016; Setiawan et al., 2018). Furthermore, the Nakamura (1989)'s paper was one of the most cited papers in publications during the 10 years after it was published (Mucciarelli and Gallipoli, 2001). Nakamura (2000) explains and proves the idea of the technique. Nakamura (2000) describes that the peak frequency of the H/V ratio is caused by the integration of SH with the formation. Rayleigh waves are not considered in the analysis even though microtremor records include surface waves. Nakamura (1989) also indicates that dynamic characteristics of the layers are the most critical controlling parameters when compared to wave propagation characteristic and radiation characteristics of soil. So, the peak frequency in H/V is the result the dynamic properties of surface layers.

The resonant frequency peak of HVSR is the result of multiple reflections and/or refractions of *horizontal shear*-waves, *SH* (Nakamura, 2000). HVSR is the dynamic transfer function of a soil deposit (Nakamura, 2000). The peak frequency, f_n, of HVSR is affected by the depth *h* to the basement/boundary where there is an extreme acoustic impedance contrast between layers (Nakamura, 2000). The peak frequency, f_n, was determined for each Nodal for different days with the following equation:

$$f_n = \frac{V_s}{4h} \tag{3.1}$$

where h is the depth, f_n, is the frequency of the peak of the HVSR. The challenge with this equation is the S-wave velocity V_s is not necessarily known within the depth of the sedimentary deposits and many researchers have used calibrated results to calculate the depth h (Stephenson et al., 2009).

3.6 Data Processing and Interpretation

The PoroTomo research team recorded ambient noise with 238 Nodals in 2016 from March 16th to 27th (Figure 3.1). We developed MATLAB algorithms for the data processing. However, since Safak (1991) indicated that the data processing has a significant impact on spectral ratios, the data processing carefully followed the following steps (Figure 3.2):

1. *Low-pass filter* was applied to the data to remove the noise from the data. Filtering is important to reduce noise level on HSVR curve (Mucciarelli and Gallipoli, 2004). As input noise level lowers in HVSR data, the filter properties - frequency, amplitude - are less resolved (Mucciarelli and Gallipoli, 2004). An increase of unfiltered noise, also, in

HVSR data causes an increase of the departure from the expected HVSR model (Mucciarelli and Gallipoli, 2004). A low-pass 20-Hz filter was applied to remove high frequency noise.

2. *H/V spectral ratio* (HVSR - Nakamura, 1989). The method basically uses three-component records of ambient noise to calculate the HVSR (Nakamura, 1989, 2000; Lermo and Chavez-Garcia, 1993, 1994):

$$HV(f) = \sqrt{\frac{P_{NS}^2(\omega f)+P_{EW}^2(f)}{P_V^2(\omega)}} \quad (3.2)$$

where HV is the spectral ratio; f represents the frequency; P_{NS}, P_{EW}, and P_V symbolize the power spectrum of two horizontal seismograms and the vertical seismogram, respectively. The resulting plot of this calculation shows some peak frequencies that indicate the resonant frequencies of the study area (Nakamura, 1989). $P_n(f)$ is the power spectrum of component n:

$$P_n(f) = \frac{1}{L}\sum_{i=1}^{L}|S_{ni}(f)|^2 \quad (3.3)$$

where L is the number of non-overlapping data windows, S is the fast Fourier transform of the n-th data window of the n-dimensional component of the Nodal sensor. Since Acerra et al. (2004) claimed that a larger number of windows yields more reliable results, 100 windows were chosen.

3. *Depth* to the bedrock surface was calculated with the determined peak frequency, f_n, and a pre-determined shear-velocity, V_s with two different approaches with the 4th step of the data processing.

4. A *S-wave velocity* distribution in the PoroTomo research area was determined by Zeng et Al. (2017)'s using and ambient noise tomography approach. S-wave velocity was used

instead of Rayleigh wave velocity since it is claimed by Volant et al. (1998) that HVSR depends on S-wave velocity. To be able to calculate the depth to the bedrock surface, we used the velocity model of Zeng et. al (2017). We modified equation 3.1 for n layer *to be able to use the S-wave velocities at 10, 20 and 30 meters (the derivation of the equation is presented in Appendix 3.A):*

$$h = \left(\frac{1}{4f_n} - \frac{h_1}{V_1} - \frac{h_2}{V_2} - \cdots - \frac{h_{n-1}}{V_{n-1}}\right) V_n + (h_1 + h_2 + \cdots + h_{n-1}) \tag{3.4}$$

where hi indicate the thickness of the different sediment layers where the S-wave velocity is considered to be constant.

Alternatively, a second method was used to calculate the depth to bedrock. In this method, a continuous S-wave velocity profile is given as a function of the vertical effective stress σ'_v distribution of the sediment layer (e.g., Santamarina et al. 2005):

$$V_s = \alpha \left(\frac{\sigma'_v}{Pr}\right)^{\beta} = \alpha \left(\frac{\gamma z}{Pr}\right)^{\beta} \tag{3.5}$$

where α (m/s) and β are experimentally determined soil parameters that are function of the soil type (Santamarina et al., 2005), γ is the unit weight of the formation (assumed constant in this study), z is the depth in the formation, Pr = 1 kPa is the reference stress. If we combine equations 3.1 and 3.5 and solve for h, we obtain the following equation (details are presented in Appendix 3.B):

$$h = \sqrt[(1-\beta)]{\frac{(1-\beta)\alpha}{4f_n}\left(\frac{\gamma}{Pr}\right)^{\beta}} \tag{3.6}$$

Based on the discrete velocity distribution presented by Zeng et al. (2018), the α and β parameters are determined. Figure 3.3 present the calculation for these parameters for the

average Vs velocity presented by Zeng et al. (2018). For the analysis, the α and β parameters were varied across the formation based on the discrete distribution of ANT S-wave velocity results. The weight γ=16 kN/m^3 was considered constant throughout the formation.

The data were processed for all Nodals sensors in the Porotomo Laboratory (Figures 3.1) to obtain the peak frequency from each HVSRs (Figures 3.4 and 3.5). We determined the peak frequency of 73 Nodals shown in Figure 3.1 for four stages. However, we chose to present the results from Stage 4 to evaluate the HVSR and calculate the depth to bedrock since we obtained more consistent results compared to the other three stages. Results presented Figures 3.5, 3.6, and 3.7 show that stage 3 (shut-down stage of the testing) tends to show very high peak frequency variation as compared to the other three stages and therefore they were discarded.

Figure 3.9 shows the elevation of the surface of the PoroTomo site. The determined peak frequencies were used to calculate the depth to bedrock with Equations 3.4 and 3.6. The estimations of the depth to bedrock for the fourth stage of the PoroTomo Experiment are shown in Figures 3.10 and 3.11. Figures 3.10a and 3.11a show the depth from the surface to the bedrock surface. Figures 3.10b and 3.11b shows the elevation of the bedrock surface.

3.7 Results and Discussion

As a result of the data gathering and processing, we attempted to obtain the depth of the bedrock of the study area. We used the HVSR method (Nakamura 1989; 2000) to determine peak frequency and interpret the depth to bedrock (Figures 3.3, 3.4, 3.5, and 3.6). We obtained the depths using two different approaches to assess the varying S-wave velocity with depth:

- A discrete profile method based on the results of ambient noise tomography by Zeng et al.'s (2016) research method.
- A continuous method based on Santamarina et al.'s (2005) power relationship between S-wave velocity and effective vertical stress.

The S-wave velocity of the PoroTomo research site was calculated for 10, 20, and 30 m depth by Zeng et al. (2017) and we used those results to calibrate the S-wave model parameters presented by Santamarina et al. (2005). We compared the results of two depths with each other and we observed approximately similar depth distributions for set of approaches with the geophones at some part of The PoroTomo site (Figures 3.10, 3.11, and 3.12). However, for most of the geophones at PoroTomo site, we had different results for two approaches. Compared to the discrete profile method based on Zeng et al.'s (2017) research, we had a deeper bedrock surface with the continuous method based on Santamarina et al.'s (2005) research (Figure 3.12).

The first challenge we faced is that the peak frequency results of some of the Nodal sensors indicated very low frequencies, an indication of very deep deposits. This problem was prevalent for the data collected on day March 16 – shutdown stage - where there is no clear peak frequency in the calculated HVSRs. The second challenge is that there was more than one peak (either two/more peak or unclear peaks) for some Nodal sensors on the HVSR results. The third challenge we faced is that there is a broad peak for some Nodals which made the detection of the peak frequency difficult.

A clear peak in spectral ration indicates that there is no other frequency band (Acerra et al., 2004). Unclear sharp peaks are observed in urban sites which have an anthropic origin – i.e. vibrating machinery - such as industrial origin. Acerra et al. (2004) recommend that the unclear sharp peaks should be eliminated from the results for interpretation. Unclear low-frequency

peaks are caused by several reasons, such as a low-frequency site that has a moderate impedance contrast at depth and/or a low level of low-frequency ambient vibrations (Acerra et al., 2004). Broad peak/multiple peaks might be the result of a sloping underground interface between softer and harder structures. Two frequency peaks may imply either a thick structure or shallow structure with very low surface S-wave velocity. They might also imply that there are two high impedance contrasts (Acerra et al., 2004).

Due to the claims of Acerra et al.'s (2004) research, we conclude that the difficulties we met could be the result of a sloping underground interface, industrial machines (the presence of the geothermal power plant and the interstate I-80 traffic), shallow underground (heterogenous deposits), low-frequency site with low-frequency vibrations (interstate I-80 traffic), and/or moderate impedance contrast (heterogenous deposits). All of these issues were found at Brady Hot Springs.

Finally, the results were summarized into contour plots of the depth to bedrock (Figures 3.10 and 3.11). The depth calculated with two equations indicates similar results. The depth calculated with Equation 3.4 (Zeng et al. 2018) tends to indicate a shallower bedrock surface as compared to the depth calculated with Equation 3.6 (Santamarina et al. 2005). Even though both models use similar depth velocities at depth equal to 5 m, 15 m, and 25 m, Santamarina's model extrapolate S-wave velocity to the surface creating lower speeds near the surface and toward the depth layers creating higher velocity in depth. These extrapolations appear to be the cause for calculated greater depths to bedrock with the Santamarina et al.'s continuous model.

3.8 Conclusions

In this study, the HVSR method (Nakamura, 1989) for the estimation of the depth of the bedrock in the Brady Hot Springs geothermal area was presented with the ambient noise data obtained by the PoroTomo research team. The ambient noise was recorded around midnight during all four stages of the PoroTomo Project; however, data from stage 4 (return of normal plat operation) was using the calculation of depth to bedrock due to greater consistency of the results.

We used the calculated velocity of the PoroTomo research site by Zeng et al. (2017) to create two different velocities models: Zeng et al. (2017)'s discrete velocity model and Santamarina et al. (2005)'s continuous velocity profile. Even though both equations gave similar results for the depth of the bedrock, the results from equation 3.6 (Santamarina et al., 2005) tend to be deeper than equation 3.4 (Zeng et al., 2018). The depth of the bedrock could in future be determined as more certain with developing technology. We compared our results with two approaches with the models of the PoroTomo project site obtained by Parker et al. (2018). The results of the continuous velocity model based on Santamarina et al.'s (2005) is similar to the results by obtained Parker et al. (2018).

3.9 Acknowledgments

The work presented herein was funded in part by the Office of Energy Efficiency and Renewable Energy (EERE), U.S. Department of Energy, under Award Number DE-EE0006760, and by the General Directorate of Mineral Research and Exploration and the General Directorate of Higher and International Education (The Republic of Turkey). The authors appreciate the PoroTomo Team for their support.

3.10 References

Acerra, C., Aguacil, G., Anastasiadis, A., Atakan, K., Azzara, R., Bard, P.Y., Basili, R., Bertrand, E., Bettig, B., Blarel, F., and Bonnefoy-Claudet, S., 2004. Guidelines for the implementation of the H/V spectral ratio technique on ambient vibrations measurements, processing and interpretation. European Commission–EVG1-CT-2000-00026 SESAME.

Crochiere, R. E. and Rabiner, L. R. (1983). *Multirate digital signal processing* (18). Englewood Cliffs, NJ: Prentice-Hall.

Faulds, J. E., Coolbaugh, M. F., Benoit, D., Oppliger, G., Perkins, M., Moeck, I., and Drakos P. (2010), Structural Controls of Geothermal Activity in the Northern Hot Springs Mountains, Western Nevada: The Tale of Three Geothermal Systems (Brady's, Desert Peak, and Desert Queen), *Geothermal Resources Council Transactions*, 34, 675-683.

Feigl, K. L. and Porotomo Team. (2017). Overview and preliminary results from the PoroTomo project at Brady Hot Springs, Nevada: poroelastic tomography by adjoint inverse modeling of data from seismology, geodesy, and hydrology. In *42nd Stanford Workshop on Geothermal Reservoir Engineering*, 15. Stanford, CA: Stanford University.

Herak, M. (2008). ModelHVSR—A Matlab® tool to model horizontal-to-vertical spectral ratio of ambient noise. *Computers & Geosciences*, 34(11), 1514-1526.

Lermo, J., and Chávez-García, F. J. (1993). Site effect evaluation using spectral ratios with only one station. *Bulletin of the seismological society of America*, 83(5), 1574-1594.

Lermo, J., and Chávez-García, F. J. (1994). Are microtremors useful in site response evaluation?. *Bulletin of the seismological society of America*, 84(5), 1350-1364.

Mihaylov, D., El Naggar, M. H., and Dineva, S. (2016). Separation of High-and Low-Level Ambient Noise for HVSR: Application in City Conditions for Greater Toronto Area. *Bulletin of the Seismological Society of America*, 106(5), 2177-2184.

Mihaylov, D., Hesham El Naggar, M., and Dineva, S. (2016). Separation of High- and Low-Level Ambient Noise for HVSR: Application in City Conditions for Greater Toronto Area. *Bulletin of the Seismological Society of America*, 106(5), 2177-2184.

Motazedian, D., Hunter, J. A., Pugin, A., and Crow, H. (2011). Development of a VS30 (NEHRP) map for the city of Ottawa, Ontario, Canada. *Canadian Geotechnical Journal*, 48(3), 458-472.

Mucciarelli, M., and Gallipoli, M. R. (2001). A critical review of 10 years of microtremor HVSR technique. *Boll. Geof. Teor. Appl.*, 42(3-4), 255-266.

Mucciarelli, M., and Gallipoli, M. R. (2004). The HVSR technique from microtremor to strong motion: empirical and statistical considerations. In *Proc. of 13th World Conference of Earthquake Engineering*, Vancouver, BC, Canada, 45.

Nakamura, Y. (1989). A method for dynamic characteristics estimation of subsurface using microtremor on the ground surface. *Railway Technical Research Institute*, Quarterly Reports, 30(1). 25-33.

Nakamura, Y. (2000). Clear identification of fundamental idea of Nakamura's technique and its applications: *Proceedings of the 12th World Conference on Earthquake Engineering*. Auckland, New Zealand, 2656.

Parker, L. M., Thurber, C. H., Zeng, X., Li, P., Lord, N. E., Fratta, D., Wang, H.F., Robertson, M.C., Thomas, A.M., Karplus, M.S. and Nayak, A. (2018). Active-source seismic

tomography at the Brady Geothermal Field, Nevada, with dense Nodal and fiber-optic seismic arrays. *Seismological Research Letters*, 89(5), 1629-1640.

Safak, E. (1991). Problems with using spectral ratios to estimate site amplification. In *Proc. of the Fourth International Conference on Seismic Zonation*, 2, 277-284.

Santamarina, J. C., Rinaldi, V. A., Fratta, D., Klein, K. A., Wang, Y. H., Cho, G. C., and Cascante, G. (2005). A survey of elastic and electromagnetic properties of near-surface soils. *Near-surface geophysics*, 1, 71-87.

Setiawan, B., Jaksa, M., Griffith, M., and Love, D. (2018). Estimating bedrock depth in the case of regolith sites using ambient noise analysis. *Engineering geology*, 243, 145-159.

Smith, S. W. (1997). Special imaging techniques. *The Scientist and Engineer's Guide to Digital Signal Processing*, 433-434.

Stephenson, W. J., Hartzell, S., Frankel, A. D., Asten, M., Carver, D. L., & Kim, W. Y. (2009). Site characterization for urban seismic hazards in lower Manhattan, New York City, from microtremor array analysis. *Geophysical Research Letters*, 36(3).

Volant, P., Cotton, F., and Gariel, J. C. (1998). Estimation of site response using the H/V technique. Applicability and limits on Garner Valley downhole array dataset (California). In Paper presented at the *XIth European conference on earthquake engineering*, Paris, 6-11.

Zeng, X., Thurber, C., Wang, H., Fratta, D., Matzel, E., and Porotomo Team. (2017). High-resolution shallow structure revealed with ambient noise tomography on a dense array. In *Proc. 42nd Workshop Geothermal Reservoir Engineering*, 13-15.

Figures

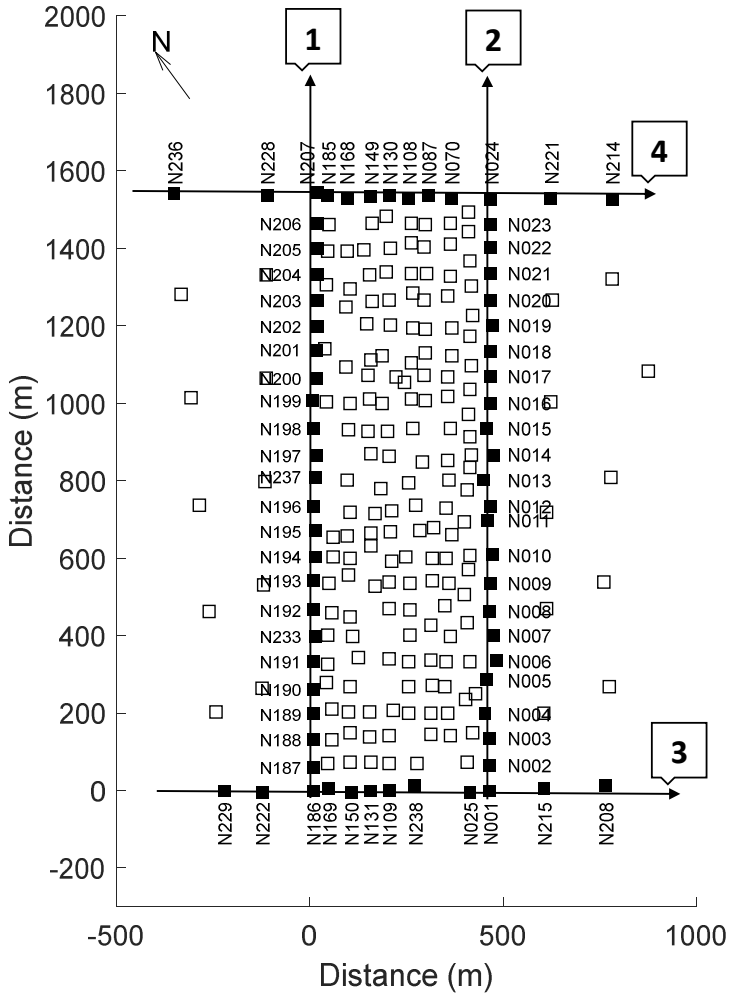

Figure 3.1 *Map of the study area. Nodal seismometers (black filled and empty squares). The filled squares show the Nodals we processed for four the four testing stages: Stage 1 - normal production, Stage 2 - shutdown, Stage 3 - pumping, and Stage 4 - back to normal production. We processed the Nodals shown with empty squares for just stage four (back to normal production).*

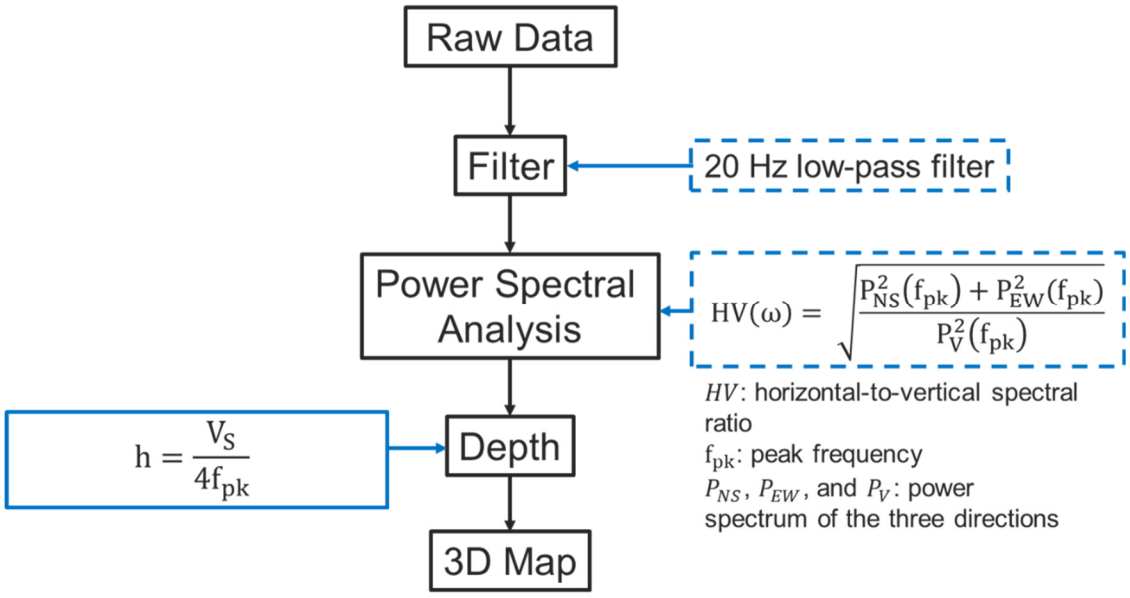

Figure 3.2 *Flow chart for data processing and interpretation.*

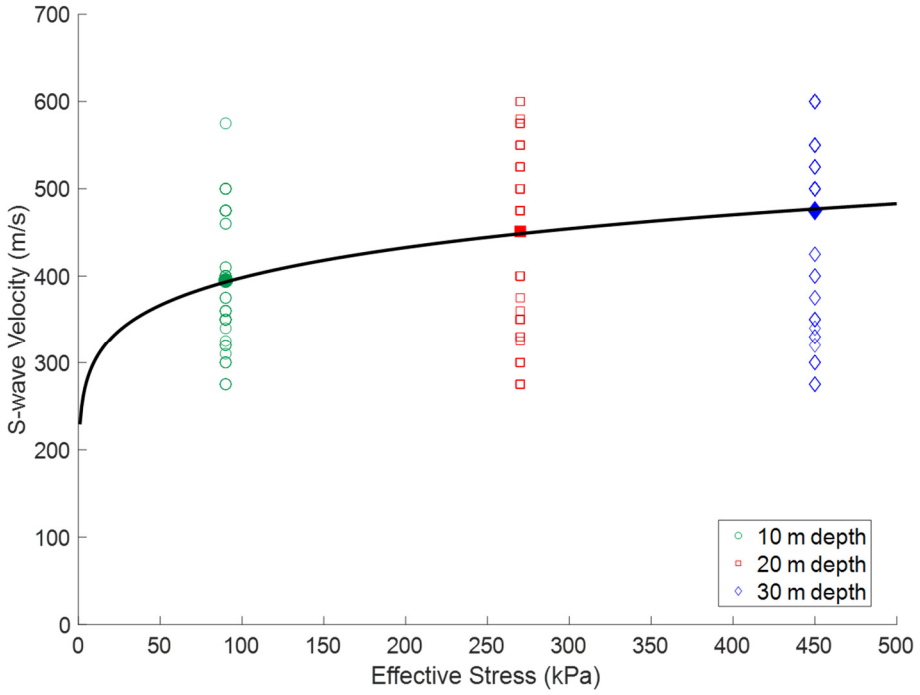

Figure 3.3 *Determination of Santamarina et al. (2005)'s S-wave velocity vs. vertical effective stress parameters using the results of Zeng et al. (2017)'s velocity model.*

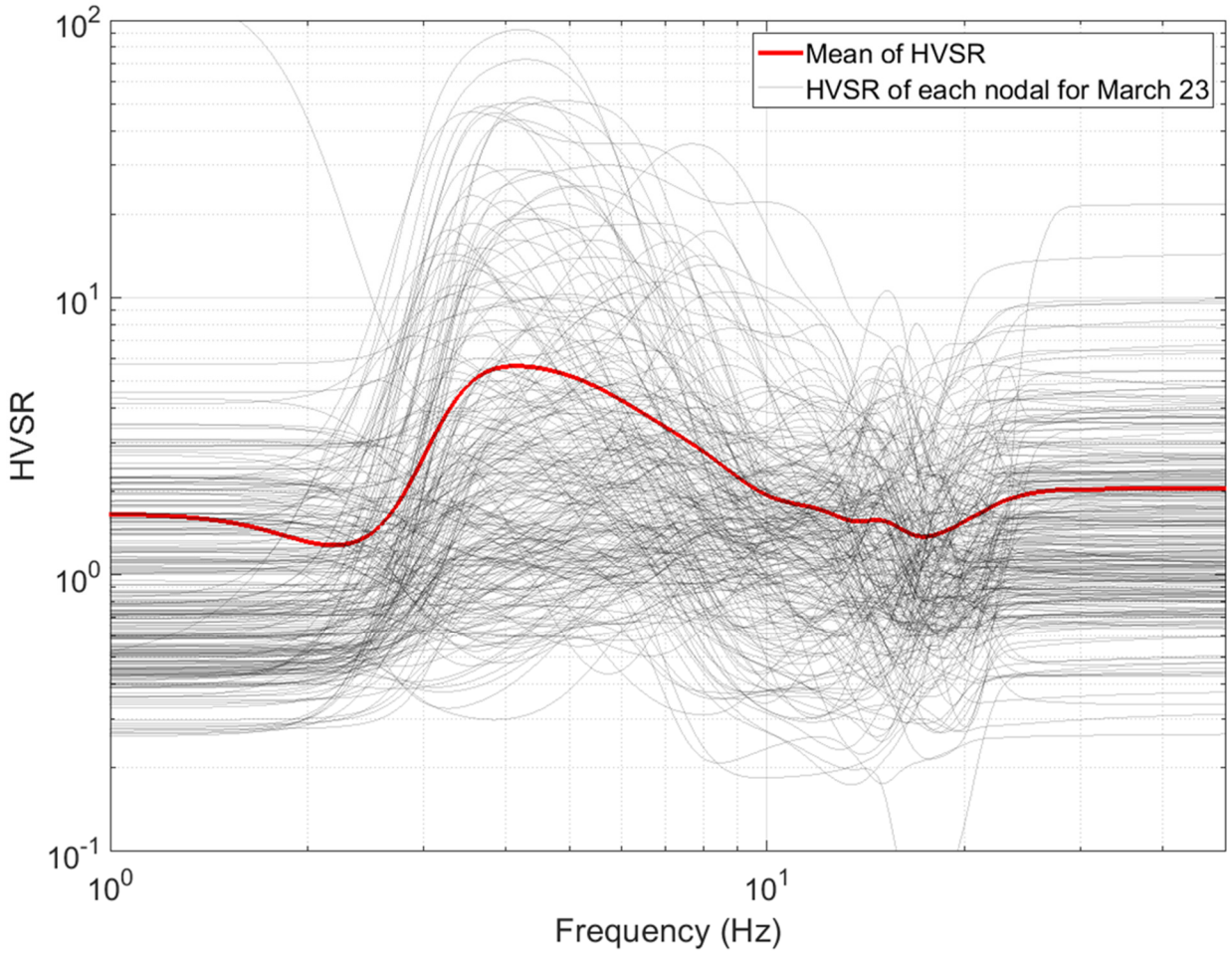

Figure 3.4 The Figure shows HVSR results of the data by Nakamura's method (1989) for the data from all Nodal of the PoroTomo site for stage four. The data are from the time from 00:00 to 01:00 am on 03/23/2016.

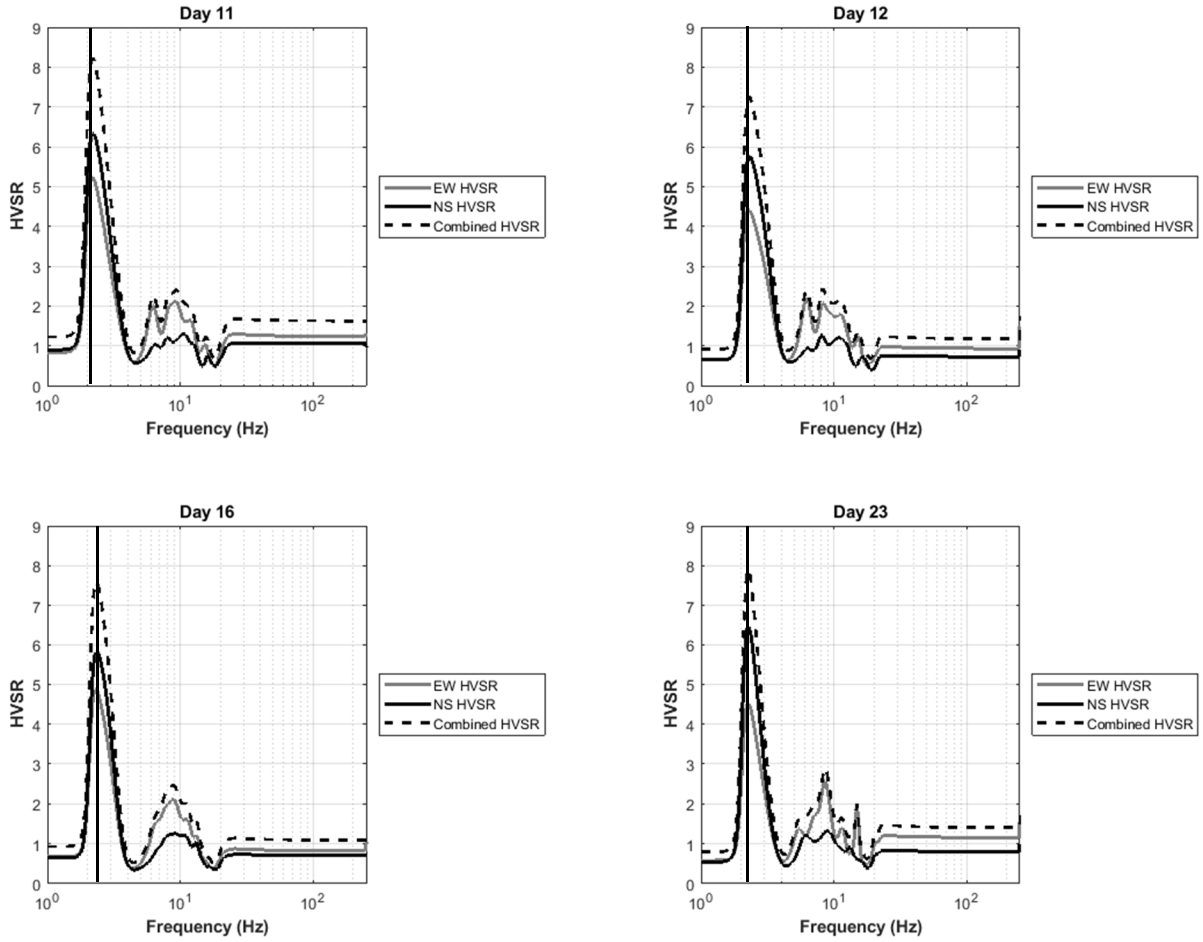

Figure 3.5 The figure shows HVSR results Nodal geophone 12. The date of the data corresponds to the easch of the four stages of the experiment.

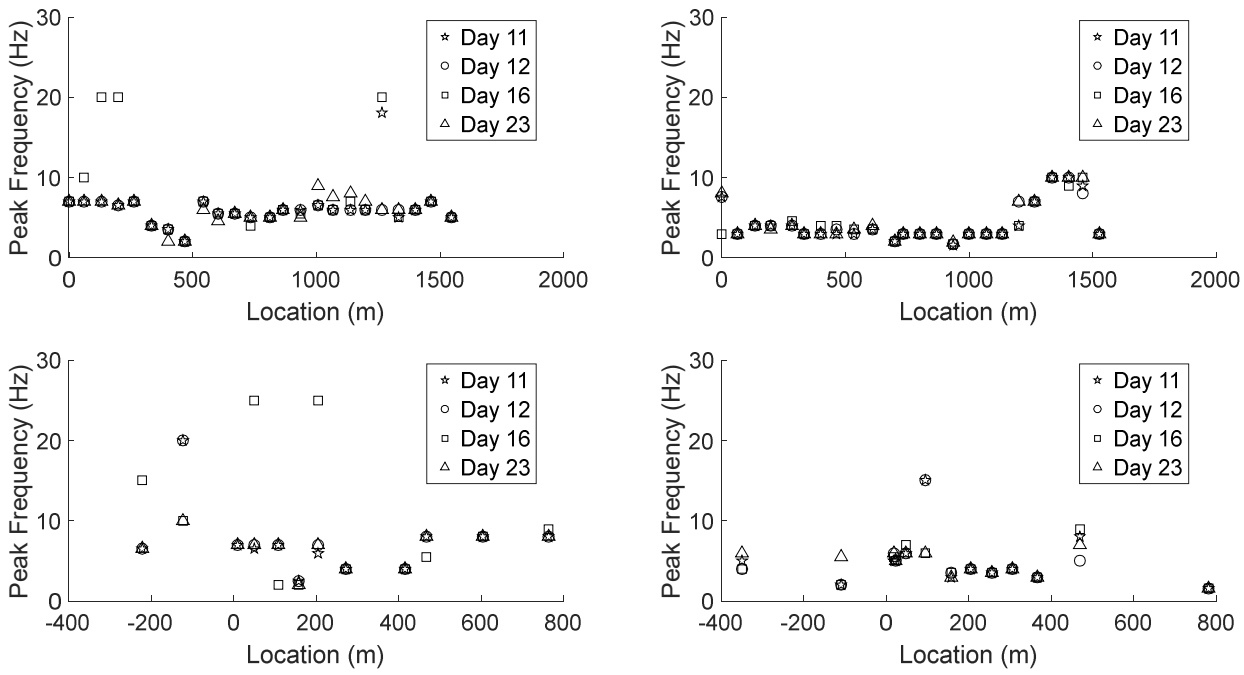

Figure 3.6 *Peak frequency for the each of stages for the four lines of Nodal arrays (Figure 3.1). Data during Stage 4 (Day March 23) provided the most consistent results. All days correspond to days in the month of March 2016.*

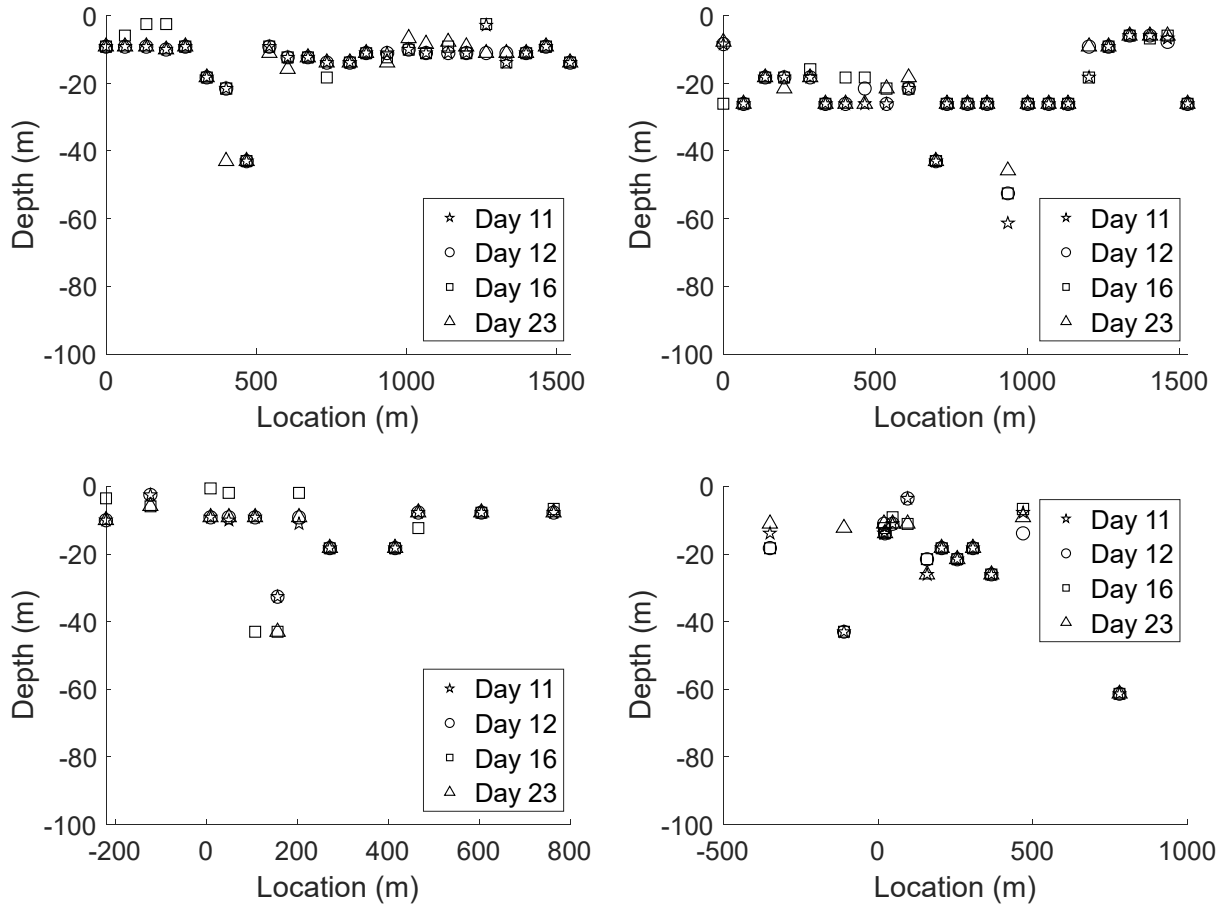

Figure 3.7 *Depth to bedrock of the PoroTomo site as the result of the Equation 3.6 (Santamarina) for the four lines of Nodal arrays Stage 4 (Day 23) provided the most consistent results. All days correspond to days in the month of March 2016.*

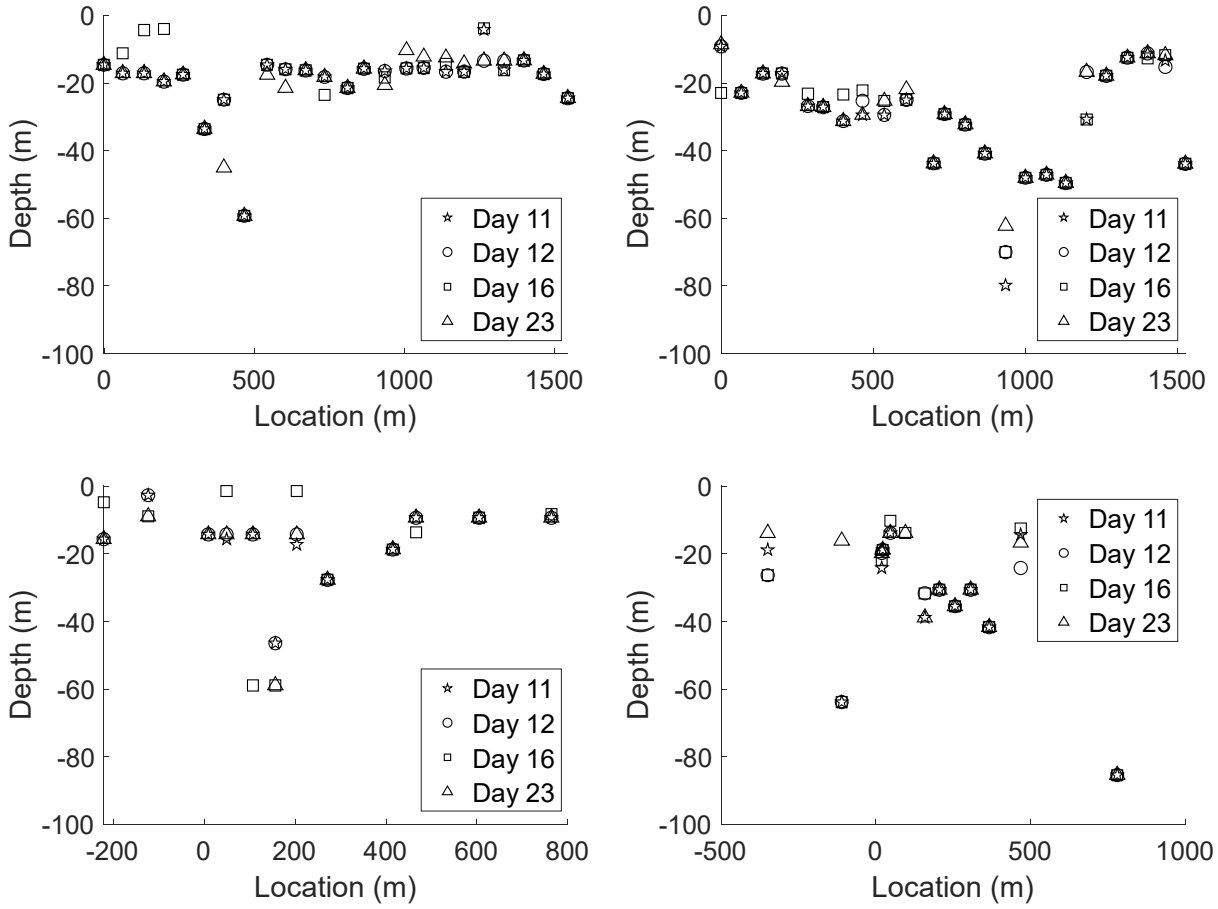

Figure 3.8 *Depth to bedrock of the PoroTomo site as the result of the Equation 3.4 (Zheng) for the four lines of Nodal arrays Stage 4 (Day 23) provided the most consistent results.*

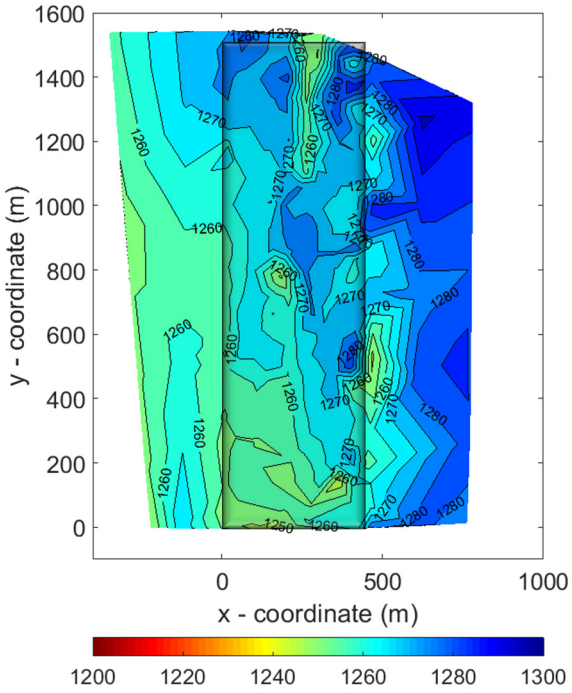

Figure 3.9 Elevation of the surface at the PoroTomo site.

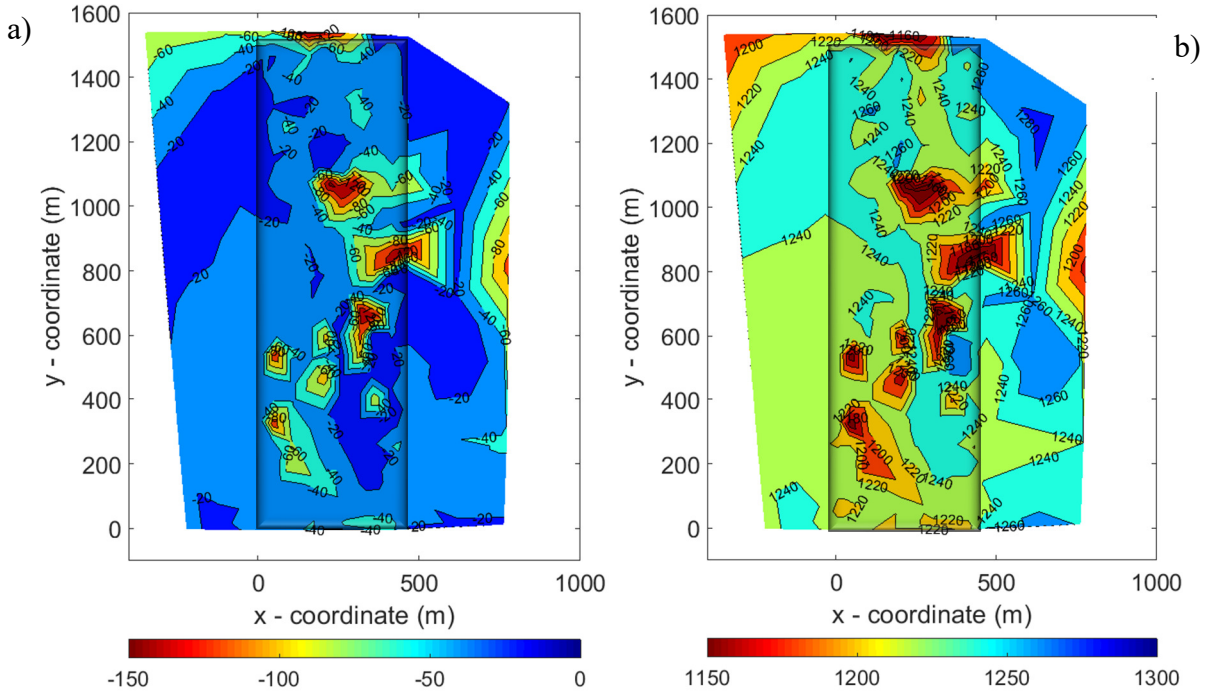

Figure 3.10 *Plot of depth calculation with Equation 3.6 (Santamarina et al. 2005). (a) Contour of the depth of the bedrock from the surface. (b) Contour of the elevation of the bedrock surface.*

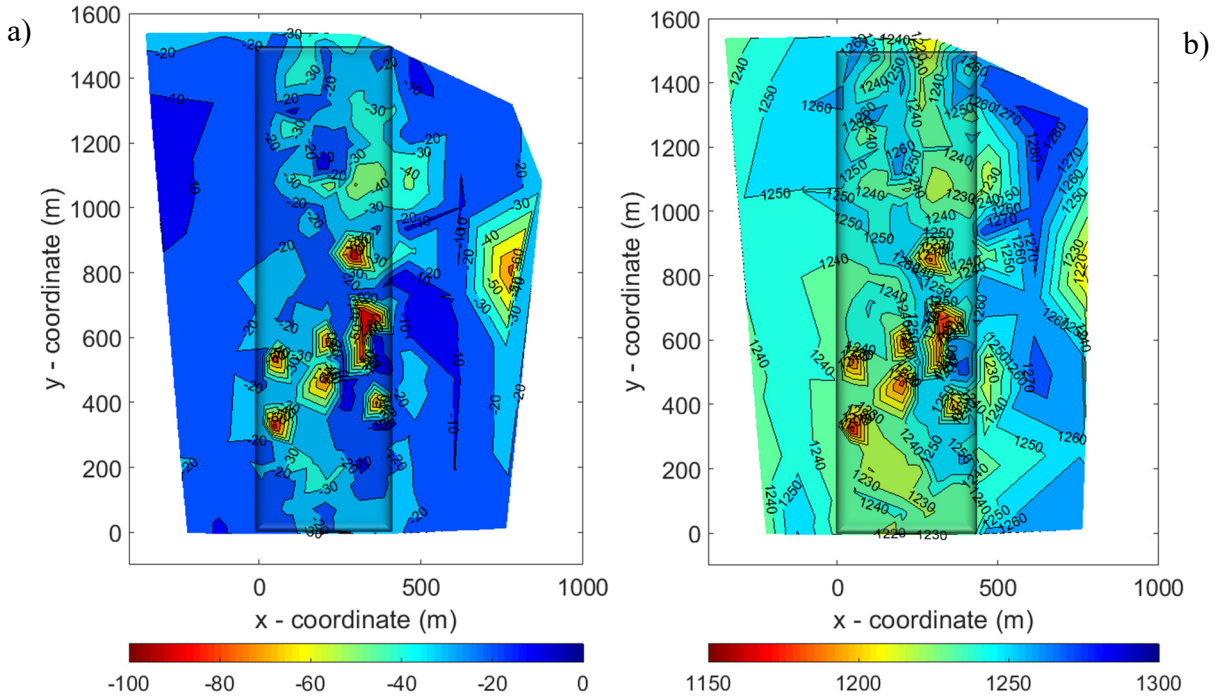

Figure 3.11 *Plot of depth calculation with Zeng et al.'s (2017) S-wave velocity model. (a) Contour of the depth of the bedrock from the surface. (b) Contour of the elevation of the bedrock surface.*

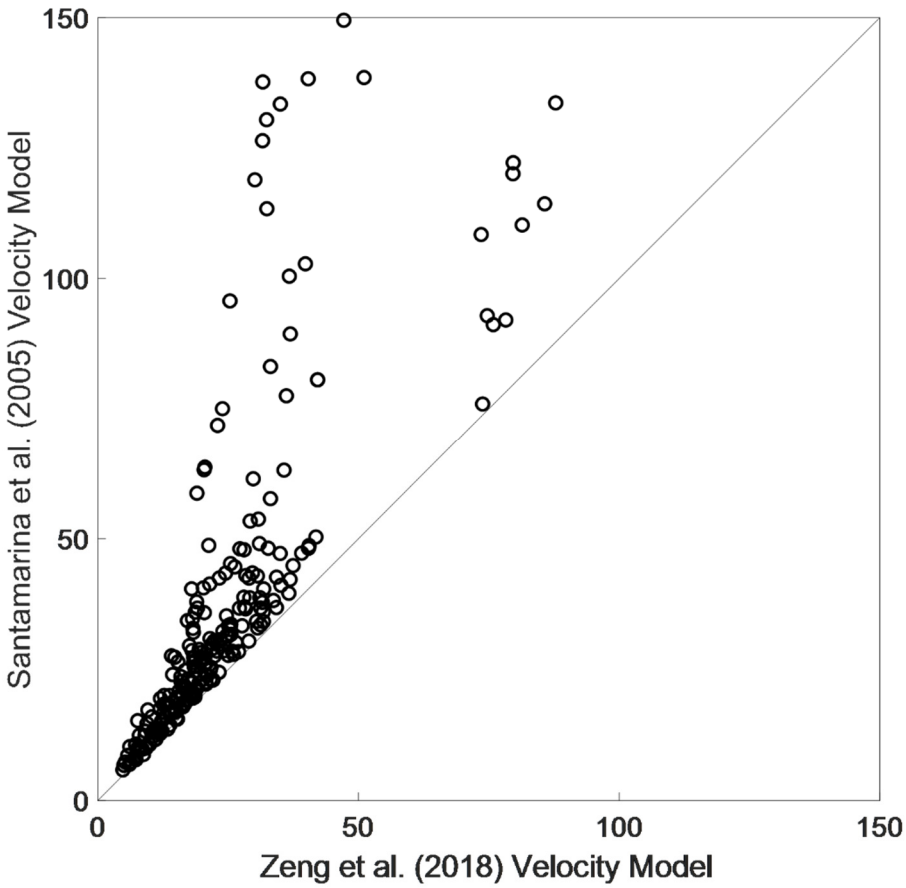

Figure 3.12 *Plot of depth to bedrock calculation with Zeng et al. (2017)'s S-wave velocity model versus Santamarina et al.'s (2005) S-wave velocity model. The Santamarina et al (2005)'s S-wave velocity model yields consistent deeper depth and the Zeng et al. (2017)'s S-wave velocity model.*

Appendix 3.A Derivation of discrete model formulation for HVSR depth determination

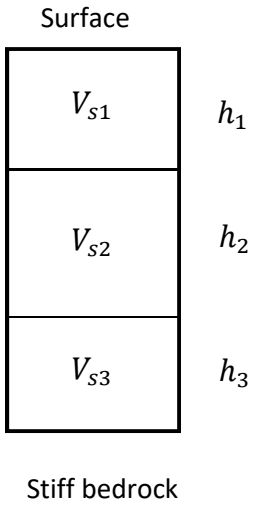

Equation 1 (Nakamura, 1989) presents the relationship between layer thickness H with S-wave velocity V_s and the peak resonant frequency f_{sk}:

$$H = \frac{V_s}{4f_{pk}} \tag{1}$$

The challenge is that the S-wave velocity is not necessarily known. To solve this problem, we propose a modification of Equation 1 that considers a discretization of thicknesses and velocity of sediment layers.

The inverse of the peak $\frac{1}{f_{pk}}$ is four time the travel time along the layers:

$$\frac{1}{f_{pk}} = 4t = 4\sum\frac{h_i}{V_i} = 4\left(\frac{h_1}{V_1} + \frac{h_2}{V_2} + \cdots + \frac{h_n}{V_n}\right) \tag{2}$$

where $h_1, h_2, \ldots, h_n$ and $V_1, V_2, \ldots, V_n$ are the thickness of each layer and their S-wave velocities, respectively. Since we do not know the thickness of the last layer, we can modify equation 2 as:

$$\frac{1}{f_s} = 4t = 4\left(\frac{h_1}{V_1} + \frac{h_2}{V_2} + \cdots + \frac{H-(h_1+h_2+\cdots+h_{n-1})}{V_n}\right) \tag{3}$$

With the modification of equation 3, we can obtain the thickness of sediment layer as following:

$$H = V_n\left(\frac{1}{4f_s} - \frac{h_1}{V_1} - \frac{h_2}{V_2} - \cdots - \frac{h_{n-1}}{V_{n-1}}\right) + (h_1 + h_2 + \cdots + h_{n-1}) \quad (4)$$

Equation 4 may be simplified for a three layer system as::

$$H = V_3\left(\frac{1}{4f_s} - \frac{h_1}{V_1} - \frac{h_2}{V_2}\right) + (h_1 + h_2) \quad (5)$$

Appendix 3.B Derivation of continuous model formulation for HVSR depth determination

Equation 1 (Nakamura, 1989) presents the relationship between layer thickness H with S-wave velocity V_s and the peak resonant frequency f_{sk}:

$$H = \frac{V_S}{4f_{pk}} \tag{1}$$

The challenge is that the S-wave velocity is not necessarily known. To solve this problem, we propose a modification of Equation 1 that consider a continuous velocity model based on Santamarina et al.'s (2005) research:

$$\mathrm{V_s} = \alpha\left(\frac{\sigma`_v}{\mathrm{Pr}}\right)^{\beta} = \alpha\left(\frac{\gamma z}{\mathrm{Pr}}\right)^{\beta} \tag{2}$$

where V_s is S-wave velocity, α (m/s) and β are the experimentally determined soil parameters (These parameters are function of the soil type - Santamarina et al., 2005), γ is the unit weight, $\sigma`_v$ is effective stress, Pr = 1 kPa is the reference stress, and z is the depth into the formation.

The travel time t along a path L is the length of the travel time in medium with varying velocity is:

$$t = \int_0^L \frac{dz}{V(z)} \tag{3}$$

Replacing Equation 2 into Equation 3 and considering that Nakamura's solution assumes that the travel path is four times the thickness of a layer, yields:

$$\frac{1}{f_s} = 4t = 4\int_0^H \frac{dz}{\alpha\left(\frac{\gamma z}{\mathrm{Pr}}\right)^{\beta}} = \frac{4}{\alpha\left(\frac{\gamma}{Pr}\right)^{\beta}}\int_0^H \frac{dz}{z^{\beta}} = \left(\frac{4}{\alpha\left(\frac{\gamma}{Pr}\right)^{\beta}}\right)\frac{H^{(1-\beta)}}{1-\beta} \tag{4}$$

Simplifying equation 4, we obtained following equation:

$$\frac{1}{f_s} = \left(\frac{4}{\alpha\left(\frac{\gamma}{Pr}\right)^{\beta}} \right) \frac{H^{(1-\beta)}}{1-\beta} \tag{5}$$

And solving for H, yields the sought equation:

$$H = \sqrt[(1-\beta)]{\frac{(1-\beta)\alpha}{4f_n}\left(\frac{\gamma}{Pr}\right)^{\beta}} \tag{6}$$

Chapter 4: Traffic Monitoring using Distributed Acoustic Sensing (DAS) at Garner Valley, California and Brady Hot Springs, Nevada

4.1 Abstract

Monitoring traffic patterns, vehicle types, and quality of road surface is important for many technical reasons. It allows for the better design of roads, the continuous evaluation of road usage, and the assessment of the state of transportation infrastructure. The number, size, weight, and speed of vehicles control deterioration rate. Furthermore, traffic noise is a potential source of seismic waves that can be used to image properties of the near surface by capturing and interpreting surface waves and coherent ambient noise. To that effect, the deployment of distributed acoustic sensing (DAS) arrays provides a new opportunity to expand the monitoring of roadway use and performance. The capability of DAS for fine spatial sampling (1 m) and rapid temporal sampling (up to 10 kHz) and its distributed nature (tens of kilometers) allows for a closer look at traffic patterns in order to assess vehicles speeds, acceleration and directions, size of vehicles, and even the quality of the roadway over long length of highways. The potential and difficulties of using DAS for these objectives were studied using two DAS arrays, one at Garner Valley in Southern California (a 700-meter array adjacent to California Highway 74) and another in Brady Hot Springs, Nevada (an 8700-meter array surrounding a Service Highway). These studies experimentally evaluated the use of DAS data for monitoring traffic and assessing the use of traffic vibration as non-localized sources for seismic imaging. This study along two highways provides a basis for examining DAS' potential and limitations as a key component of intelligent highway systems.

Key Words: DAS; Rayleigh wave; Traffic noise; Near-surface seismic tomography

4.2 Introduction

Distributed acoustic sensing (DAS) is a developing and advantageous technology that records seismic signals by sending laser pulses along a fiber-optic cable while monitoring Rayleigh backscattering (Daley et al., 2013; Mateeva et al., 2012; Moleenar et al., 2012; Webster et al., 2013; Parker et al., 2014; Hornman, 2017; Wang et al. 2018). DAS can potentially have thousands of sensors permanently used in the subsurface, and in doing so, become cost-effective (Daley et al., 2013). Moreover, since the changes in the environment affects the optical backscatter, it is the basis of why the fiber-optic cables are deployed as continuous array of sensors with very small sampling in both space (about 1 meters) and time (higher than 10 kHz - Daley et al., 2013).

Monitoring traffic is important for a number of reasons. It allows for better design of future roads, evaluates current usage, and helps in assessing the quality of the road surface. Understanding the number, speed, size, and weight of vehicles on the roadways helps understanding the current state of the infrastructure. Also, real-time information supplies data to intelligent information systems such as electronic road signs saving the user time and cost, and potentially helping the environment. The earliest traffic monitoring was done in the 1920s using a pneumatic road tubes, which are still in use today due to its low cost and simplicity. However, the pneumatic road tubes only counts vehicle, and by themselves alone cannot estimate the type and weight of vehicles or the speed or direction of the traffic. Since these early developments, a number of different traffic monitoring techniques have been used (Gardner 2000), including wireless sensor networks (Mittal and Bhatia, 2010; Pascale et al, 2012) and passive infrared/ultrasonic sensing (Mousa et al., 2015). One reason for traffic monitoring is to obtain real-time output for alerts or electronic road signs. Video monitoring allows for the extraction of traffic loads, lane changes, and average velocities (Semertzidis et al. 2009), however video

monitoring cannot estimate whether the vehicle is loaded or not. Video monitoring also has issues resolving different types of moving objects because of the presence of lights from the vehicles of the number of the vehicles because of poor weather conditions. Finally, video surveillance faces challenges in weak or rapidly changing lighting or in the shadows (Ji et al., 2006). New studies have focused on improving the current systems. For example, Ji et al. (2006) developed a background subtraction method, one of a few different ways traffic may be detected in videos, to help in poor lighting or shadows. Zhou et al. (2007) developed an algorithm that can be trained to work in shadows and poor illumination conditions. Chen et al. (2011) created a real-time vision system for night-time traffic monitoring that detects vehicle headlights and taillights and groups them into vehicles.

Even more recently, there have been studies looking at monitoring seismic signals created by traffic. Vibrations from traffic are not sensitive to the same issues, such as weather and poor visibility, which hamper video monitoring systems. Riahi and Gerstoft (2015) have used an array of 5200 geophones in a 7 km by 10 km area in Long Beach, CA to monitor train, air, and car traffic. They were also able to monitor local rail track traffic, aircraft landing at a nearby airport, and nighttime traffic on Interstate I-405.

Traffic monitoring using seismic waves can be used to obtain information about the road conditions. Eriksson et al. (2008) referred to a technique that was named “Pothole Patrol” to monitor road conditions and locate potholes in urban setting. Eriksson et al. (2008) deployed GPS receivers attached to taxis (used as sources) and accelerometers (used as sensors) to identify areas along the roads and streets where there were issues related to road maintenance. Using the “Pothole Patrol”, Eriksson et al. (2008) were able to identify potholes or damaged pavements areas that caused high vibrations and needed attention. They rated their success rate at 90%.

Mohan et al. (2008) used smartphones to monitor both traffic conditions and road conditions in urban areas in developing countries where traffic patterns are not as organized. Mohan et al. (2008) developed a different application: TrafficSense. TrafficSense uses the smartphone's sensors (e.g., accelerometer, microphone, GSM radio, and/or GPS receiver) to monitor for vibrations created when traffic hit potholes, the sounds of honking horns, and braking noise of the interrupted traffic.

Traffic monitoring is also important in border control operations. Coulter et al. (2011) utilized light aircraft and unmanned aerial vehicles for repeat imaging of a border region and were able to identify image changes that occurred when a vehicle or person was present. Kirkendall et al. (2007) and Owen et al. (2012) have used a Distributed Acoustic Sensing (DAS) array to monitor borders and pipelines. DAS uses a fiber-optic cable connected to an interrogator box, laser pulses, and Rayleigh scattering to measure strain or strain rate every meter, with gauges averaging length of around 10 m for distances up to 100 km and at sampling rates as fast as 100 kHz (Johannessen et al. 2012; Miller et al. 2012). Kirkendall et al. (2007) used a DAS array to capture the vibration of a person walking perpendicular to the fiber optic cable and as a passing convoy of light trucks. Akerly (2018) discussed an exploratory program using DAS for the monitoring of a section of I-29 in Fargo, North Dakota. The system was deployed to monitor traffic speed and to assess vehicle types.

Besides monitoring traffic strictly for traffic information or border control, some studies use traffic as a seismic source. Dilemen et al. (2015) used traffic to estimate near-surface attenuation properties. They compared attenuation results from traffic-generated waves to results from earthquake-generated waves and found a similar attenuation using both wave types. Nakata (2016) imaged S-wave velocity distribution in the near surface by capturing and interpreting

Rayleigh and Love waves from traffic noise with an array of up to 100 geophones. Zeng et al. (2016, 2017) used the same DAS array and data from this study to calculate noise cross-correlation functions (NCFs) for one-minute intervals and applied Multichannel Analysis of Surface Waves to determine the phase velocity dispersion. The dominant noise in the data was attributed to traffic. The dispersion curves calculated by Zeng et al. (2016 and 2017) compared well with those from active sources calculated by Lancelle et al. (2016).

Wellbrock et al. (2019) successfully used fiber sensing system for the first time to determine vehicle speed, vehicle flow, and road conditions such as pavement deterioration on the roads like potholes by using monitoring traffic noise. They used telecommunication fiber for the measurements and were able to show with the help of artificial intelligence vehicle speed and roadway surface influences the collected DAS data. However, Wellbrock et al. (2019) were not able to identify the vehicle type from the collected data nor they controlled the geometry of the array to monitor how different array configurations can capture different signatures.

This study evaluates the use of DAS for monitoring traffic. The high spatial sampling and distributed nature of DAS allows for a closer look at the traffic as it passes and how the speed of the vehicle may change over the length of the array. This chapter focuses on 1) counts of passing vehicles, 2) relative amplitudes between those vehicles, 3) speeds and directions, and 4) evaluation of roadway surface based on the analysis of traffic events from two study areas, one in Southern California (Garner Valley) and another one in Northwestern Nevada (Brady Hot Springs Geothermal Field).

4.3 DAS Data Acquisition

The first field site used in this study was the Garner Valley Downhole Array operated by University of California-Santa Barbara. It is located 21 km southwest of Palm Spring, CA. The site is mostly flat-lying alluvium above weathered and unweathered granitic bedrock (Youd et al. 2004). The site was instrumented with 762 meters of fiber optic cable trenched approximately 0.3 m deep in a rectangular array with two interior diagonal segments (Figure 4.1). The overall size of the array is an approximately 160 m by 80 m rectangle with two internal crosshatch lengths. One of the long legs of the rectangle is next and parallel to California State Highway 74 (the leg is label Long Line II in the figure). The DAS channels along Long Line form a 140 m long and continuous seismic array for the traffic signals created by vehicles traveling along local highway. The primary focus of this study is on the passive sources in the evening. The sampling rate of the DAS data were down sampled to 500 samples per second from 1 kHz.

The second field site is the PoroTomo Project in the Brady Hot Springs geothermal field about 70 miles east of Reno, NV (Feigl et al. 2017). The PoroTomo Project deployed fiber optic cables for traffic monitoring with Distributed Acoustic Sensing (DAS) to monitor the near-surface of Brady Hot Springs. The near surface geology is composed of heterogeneous alluvial sediments and thermal fumaroles. A 8700-meter long fiber optic cable was trenched to a depth ranging between 0.3 m and 0.45 in a zig-zag pattern (Figure 4.2). The fiber optic cable array was located south-east side of the I-80 highway and crosses a service road that runs parallel to the I-80 highway. The fiber optic array had about 8600 of sensing DAS channels. The spatial resolution of the DAS cable was 1 m and the temporal sampling of the cable was 200 Hz which was down sampled from 1 kHz collected DAS data. For this study use the channels shown by the stars in Figure 4.2. By using only those channels, the array is not continuous, and the channels

behave as point sensors. The work in Brady Hot Springs also included video monitoring of the traffic during the DAS data collection, in doing so, we know what kind of vehicle was passing on the road during the DAS data record.

4.4 Data Processing Procedure

The recorded continuous data of both research sites was processed with MATLAB with the following steps:

1. *A band-pass filter* was deployed to filter the data between 2-80 Hz for Garner Valley and 3-25 Hz for Brady Hot Springs since the main frequencies associated with traffic are between the frequencies we mentioned for our data. Two samples of 15-minute data traces from DAS channels parallel to the highway at Garner Valley are plotted in Figure 4.3 and one example of ~27 minutes of data from Brady Hot Springs is plotted in Figure 4.4.
2. *Vehicle Counts:* The data presented in Figure 4.3 shows two 15-minute time periods of DAS data recorded along Long Line II parallel to California Highway 74 at Garner Valley (Figure 4.1). The recording starting at 8:24:19 PM local time shows 11 events while the recording starting at 8:39:24 PM shows 10 events. Figure 4.4 shows a ~27-minute time period recorded by the channel 8553 at Brady Hot Springs (Figure 4.2). Recoding starts at 6:41:22 AM local time to coincide with the rush hour of workers going to nearby diatomaceous earth mine. There are 11 events in this data set.

4.5 Results

Traffic Monitoring. Looking at a single channel does not allow for separation of multiple vehicles passing the channel at the same time (e.g., DAS data from channel 8553 in Figure 4.4).

However, the spatial sampling of a DAS array allows for multiple points of reference to be evaluated for the number of passing vehicles. Figures 4.3 and 4.5 show data from the channels along the line running parallel to the road as mentioned in Figure 4.1 (California Highway 74 - Garner Valley) and Figure 4.2 (Service Road - Brady Hot Springs). Using this method allows for individual vehicles to be tracked as they travel along the highway.

The data presented in Figure 4.4 includes two vehicles that are travelling together (between 0 – 100 seconds). These two vehicles appear as just one event at channel 5258, while looking at a number of channels (channel 7145 and 7430) they can be seen as multiple vehicles. The use of multiple channels helps in correctly identifying the number of vehicles. The first vehicle in the 30-minute window is an example of this in Figure 4.5. As seen in Figures 4.3 and 4.5, the two vehicles passing in opposite directions are easily identifiable as separate vehicles since one vehicle arrives after the other in some channels even though they are inseparable for some other channels since they arrived at that channel location at the same time. This is one of the clear advantages of using data from a high density set of sensors as allowed by DAS.

DAS arrays can also be successfully used to count passing vehicles when the vehicles are spaced out enough in time to identify them as separate events (the resolution is improved when the sensor are located closer to the roadway). However, some events cannot be separated in the data and do not give an indication whether DAS could be successfully used to monitor traffic on much busier roads or on highways where multiple lanes of traffic are passing. Future work involving different sensor arrays and analysis of DAS data where more frequently passing vehicles are prevalent would be required to better assess DAS capabilities or provide plans for different type of deployments.

Relative Amplitudes: As is evident in Figures 4.3 (Garner Valley) and Figures 4.4 and 4.5 (Brady Hot Springs) not all passing vehicles yield the same signal amplitude. One possible reason for the difference in amplitudes relates to the direction the vehicle is traveling and thus the distance between the vehicle and the receiver. Vehicles traveling southeast-bound are traveling on the side of the road closer to the DAS line than vehicles traveling northwest-bound in Garner Valley, so it would be logical that their amplitudes and energy signal would be higher than those of a vehicle traveling on the other side of the road if everything else was held constant (see Figure 4.6). Another possible reason for the difference in amplitudes between vehicles is due to vehicle size as seen in Figure 4.7 (Brady Hot Springs). A relatively larger vehicle should make a larger amplitude signal. However, this possibility could not be investigated at Garner Valley because there was not a camera recording traffic. For Brady Hot Springs data, however, there was video recording. The highest amplitude event shown in Figure 4.7a corresponded to a semi-tractor trailer and shown in Figure 4.7b corresponded to SUVs. That signature from truck (Figure 4.7a) was much larger than the amplitudes yielded by cars and SUVs traveling along that service road. Also, the signature from SUVs (Figure 4.7b) was larger than the amplitudes and energy signal yielded by small cars traveling along the service road.

Vehicle Speeds: DAS data can be used to calculate the speed of the passing vehicles. By analyzing the moveout caused by vehicles along the DAS line in Figures 4.3 and local DAS sensors in Figure 4.5 the speed of travel of those vehicles can be calculated. The speeds of the events are shown on Figures 4.3 and 4.5 for both sites. Speeds vary between 16 m/s to 32 m/s for Garner Valley for two data sets shown in Figure 4.3 (Table 4.1 summarizes the speeds of the traveling vehicles directions). Speeds ranged from 16 m/s to 36 m/s for Brady Hot Springs (Table 4.2 summarizes the speeds of the traveling vehicles directions).

Figure 4.8 shows a more detailed example of two vehicles, one traveling each direction, and the speed calculation associated with them along California Highway 74 in the Garner Valley site. The traces show multiple sets of events with different arrival times and different levels of coherence. The event indicated by the inclined straight black dashed line show the average slope used for the speed calculation; 24 m/s for Figures 4.8a. We also see arrivals in Figures 4.8a and 4.8b that are coherent and are possibly due to potholes/irregularities and two bumps at the end and the beginning of the bridge on the roadway surface shown Figure 4.8b (these bumps are known as the 'the bump at the end of the bridge' - Garnier Villarreal, 2016). The moveout for these events were calculated as the travel time (distance from the road to the each of the channels) caused by a point source on the roadway just next to the DAS array (the modeled time arrivals are shown with curved red line in Figures 4.8a and 4.8b). The wave speed of the events from the potholes was assumed to be 220 m/s and the apparent wave velocity of the events from the bumps at the bridge was determined to be 225 m/s. While the same wave velocity should have been expected for all set of the events (i.e., same surface wave velocity), the slight misalignment of the bridge with respect to the Long Line II shield a sight higher apparent velocity.

4.6 Discussion

Vehicle Count. The DAS results for vehicle counts indicate that DAS can be successful in counting vehicles traveling in opposite directions. Individual vehicles are identifiable when a line of multiple DAS channels is used, and the same vehicles may have been confused if only point receivers at the beginning and end of the line were used. Even when one channel could not separate two vehicles, the use of consecutive channels allows for separation of two distinct

vehicle events. However, the study in Garner Valley does not test the ability of DAS to identify individual vehicles in high-density traffic areas. The vehicles, which were appeared as one vehicle at one channel, were separated by several seconds at another channel before they were considered two separate vehicles. If there were many more vehicles arriving at channels at the same time, separating the vehicles may not be possible and this could be a possible aspect for future study for the arrangements and geometry of arrays. The use of zigzagging at Brady Hot Springs and the selection of the corner channels might have favored the collection of data right when the vehicle is passing by on roadway. Furthermore, having video recording of the traffic at Brady Hot Springs made the data interpretation easier compared to the Garner Valley data since we were able to justify some of the observed events.

Vehicle Speeds. Vehicle speeds are calculated using DAS data by following the slope of the traffic signal across multiple channels. When using that slope the assumption that the cable and highway are parallel at the Garner Valley site was made. However, the DAS cable and the California Highway 74 are not parallel to each other. That is, there is a small angle between the road and the DAS line but it is not expected to change the velocities by a significant amount. All passing vehicle signals arrive at the DAS with surface wave speed and the difference in the distance will create a small error in the speed determination (Lancelle 2016). This systematic error will tend to increase the calculated speed of the NW-bound vehicles and it will tend to decrease the calculated speed for the SE-bound vehicles. Lancelle (2016) suggested that the error is on the order of 5%.

One benefit of the high spatial sampling of DAS is that there are multiple points of measurement over extended distances. Over the approximately 140 m of the length of cable on Long Line II, all vehicles in the 15-minute window traveled at a fairly consistent speed, even

when channels two meters apart were plotted. Still, tracking vehicles slowing down or speeding up should be possible, since a curve or gradual change in slope would be seen in the Garner Valley site area. It should be possible to follow the acceleration and deceleration of a vehicle and the speed at which vehicles accelerate or decelerate. This could give an indication of accidents or traffic jams on a road. Some indication of these changes in vehicles speeds can be seen in the data presented in Figure 4.5. While we calculated constant speeds, there are some misalignments in between the constant speed slope and the events. This type of analysis could be a topic of future study using DAS data.

Roadway Surface. There some events that show other coherent arrivals but are not specifically related to a vehicle traveling along highway. Figure 4.6 (events #1 and 3 in Figure 4.3 – Garner Valley) and Figure 4.7 (event #11 in Figure 4.3 – Garner Valley) and show one passing vehicle, that shows multiple arrivals. The case of point sources in the roadway (e.g., potholes) was discussed in the previous section. However other events are observed and hypothesized. Figure 4.7 shows another cause for the observed vibrations. One possible cause for those sets of arrivals is the 'bump at the end of the bridge'. This 'bump' appears when a car hits the sudden change of slope at the approach between the road and a bridge (Garnier Villarreal, 2016). Because the bridge is just east of the DAS line parallel to the highway (Figure 4.1), the wave arrivals will have the speed of surface waves (~255 m/s – higher than the surface wave due to the misalignment of the cable with the bridge). Other events appear to be caused by additional potholes in the roadway.

Undefined Events. Figure 4.9a shows the events the same as the events in Figure 4.3 along four lines: long line I, long line II, short line I, and short line II. Although we can see changes in the arrival times for all events except event 8, we cannot observe any change for the

arrival times shown as event 8. We thought it could be a seismic event. However, we could not capture moveouts across the array. So, that source of that event remains unknown.

4.7 Conclusions

We deployed two DAS arrays to monitor traffic patterns and evaluate the quality of the roadway surface next to California Highway 74 at Garner Valley and next to a service road at Brady Hot Springs. In addition, two digital cameras recorded video of traffic along the service road at Brady Hot Springs. With the data from both sites, a count of passing vehicles was obtained and the direction, number, speed, and size of each of the vehicles was determined. Identification of overlapping vehicles was successfully done, and relative amplitudes gives an indication of distance from the cable. Further work could be done to evaluate the ability of DAS to monitor traffic when multiple lanes of traffic are present or in high traffic areas. Finally, seismic signal created passing vehicles could be used to obtain perform Spectral Analysis of Surface Waves (SASW) and image S-wave velocity distribution at the near-surface.

4.8 Acknowledgements

The work presented in this research was financially supported by the Office of Energy Efficiency and Renewable Energy (EERE), U.S. Department of Energy, under Award Number DE-EE0006760. Moreover, the author, Esra Ak, was funded by the General Directorate of Mineral Research and Exploration and the General Directorate of Higher and International Education (The Republic of Turkey) as a graduate student at University of Wisconsin - Madison. Lastly, the authors appreciate the PoroTomo Team for their support.

4.9 References

Akerly (2018). “Distributed Acoustic Sensing (DAS) Along I-29 for Traffic Monitoring”. URL: https://www.fhwa.dot.gov/innovation/stic/20180419_nddot_das_project.pdf [Accessed on December 18, 2018].

Brittle, K. F., Lines, L. R., and Dey, A. K. (2001). Vibroseis deconvolution: a comparison of cross-correlation and frequency-domain sweep deconvolution. Geophysical Prospecting, 49(6), 675-686.

Cerutti-Maori D., Klare J., Brenner A. R., and Ender J. H. G. (2008) "Wide-Area Traffic Monitoring With the SAR/GMTI System PAMIR," in *IEEE Transactions on Geoscience and Remote Sensing*, vol. 46, no. 10, pp. 3019-3030.

Daley, T. M., Freifeld, B. M., Ajo-Franklin, J., Dou, S., Pevzner, R., Shulakova, V., Kashikar, S., Duo, S., Lindsey, N., Wagner, A. M., Daley, T. M., Freifeld, B., Robertson, M., Peterson, J., Ulrich C., Martin, E. R., and Ajo-Franklin, J. B. (2017). “Distributed Acoustic Sensing for Seismic Monitoring of The Near Surface: A Traffic-Noise Interferometry Case Study”. Scientific Reports. 7: 11620, DOI:10.1038/s41598-017-11986-4

Eriksson, J., Girod, L., Hull, B., Newton, R., Madden, S, and Balakrishnan, H. (2008). “The pothole patrol: using a mobile sensor network for road surface monitoring” *MobiSys '08 Proceedings of the 6th international conference on Mobile systems, applications, and services,* 29-39, URL http://nms.csail.mit.edu/papers/p2-mobisys-2008.pdf [Accessed on June 1, 2019]

Feigl, K. L. and the PoroTomo Team (2017). Overview and preliminary results from the PoroTomo project at Brady Hot Springs, Nevada: poroelastic tomography by adjoint inverse modeling of data from seismology, geodesy, and hydrology. In 42nd Stanford

Workshop on Geothermal Reservoir Engineering (p. 15). Stanford, CA: Stanford University.

Gardner M. P. (2000). Highway traffic monitoring. *Transportation Research Board. Transportation in the new millennium*, 5.

Hornman, J. C. (2017). Field trial of seismic recording using distributed acoustic sensing with broadside sensitive fibre-optic cables. *Geophysical Prospecting*, 65(1), 35-46.

Ji, X., Wei, Z., and Feng, Y. (2006). Effective vehicle detection technique for traffic surveillance systems. *Journal of Visual Communication and Image Representation*, 17(3), 647-658.

Johannessen K., Drakeley B., and Farhadiroushan M. 2012. Distributed Acoustic Sensing - a new way of listening to your well/reservoir, SPE Intelligent Energy International held in Utrecht, The Netherlands, 27–29 March 2012, SPE 149602, pp. 9.

Kirkendall C.K., Bartolo R., Salzano J., Daley K. (2007) "Distributed Fiber Optic Sensing for Homeland Security", 2007 NRL Review.

Mateeva, A., Mestayer, J., Cox, B., Kiyashchenko, D., Wills, P., Lopez, J., Grandi, S., Hornman, K., Lumens, P., Franzen, A., and Hill, D. (2012). Advances in distributed acoustic sensing (DAS) for VSP. In *SEG Technical Program Expanded Abstracts 2012* (pp. 1-5). Society of Exploration Geophysicists.

Meyer F., Hinz S., Laika A. and Bamler R., 2005. A-Priori Information Driven Detection of Moving Objects for Traffic Monitoring by Spaceborne SAR. In: Proc. of CMRT05, International Archives of Photogrammetry, Remote Sensing and Spatial Information Sciences, Vol. XXXVI, 3/W24, pp. 89–94.

Miller, D., Parker, T., Kashikar, S., Todorov, M., and Bostick, T. (2012, June). Vertical seismic profiling using a fibre-optic cable as a distributed acoustic sensor. In 74th EAGE Conference and Exhibition incorporating EUROPEC 2012, pp. 5.

Miller, D.E., Goetz, J., Hennings, J., and Lueth, S. (2013). Field testing of fiber-optic distributed acoustic sensing (DAS) for subsurface seismic monitoring. *The Leading Edge*, 32(6), 699-706.

Mittal, R., and Bhatia, M. S. (2010, December). Wireless sensor networks for monitoring the environmental activities. In *2010 IEEE International Conference on Computational Intelligence and Computing Research* (pp. 1-5). IEEE.

Mohan, P., Padmanabhan, V. N., and Ramjee, R. (2008). "Nericell: rich monitoring of road and traffic conditions using mobile smartphones". Proceedings of the 6th ACM conference on Embedded network sensor systems, 323-336. ACM.

Molenaar, M. M., Hill, D., Webster, P., Fidan, E., and Birch, B. (2012). First downhole application of distributed acoustic sensing for hydraulic-fracturing monitoring and diagnostics. *SPE Drilling & Completion*, 27(01), 32-38.

Moschetti, M. P., Ritzwoller, M. H., and Shapiro, N. M. (2007). Surface wave tomography of the western United States from ambient seismic noise: Rayleigh wave group velocity maps. *Geochemistry, Geophysics, Geosystems*, 8(8).

Mousa, M., Oudat, E., & Claudel, C. (2015, October). A novel dual traffic/flash flood monitoring system using passive infrared/ultrasonic sensors. In 2*015 IEEE 12th International Conference on Mobile Ad Hoc and Sensor Systems* (pp. 388-397). IEEE.

Parker, T., Shatalin, S., and Farhadiroushan, M. (2014). Distributed Acoustic Sensing–a new tool for seismic applications. *First break*, 32(2), 61-69.

Pascale, A., Nicoli, M., Deflorio, F., Dalla Chiara, B., & Spagnolini, U. (2012). Wireless sensor networks for traffic management and road safety. *IET Intelligent Transport Systems,* 6(1), 67-77.

Riahi, N., and Gerstoft, P. (2015). "The seismic traffic footprint: Tracking trains, aircraft, and cars seismically". *Geophysical Research Letters*, 42(8), 2674-2681.

Semertzidis, T., Dimitropoulos, K., Koutsia, A., and Grammalidis, N. (2010). "Video sensor network for real-time traffic monitoring and surveillance". *IET intelligent transport systems*, 4(2), 103-112.

Wang, H., Fratta, D., Lord, N., Zeng, X., and Coleman, T. (2018). Distributed acoustic sensing (DAS) field trials for near-surface geotechnical properties, earthquake seismology, and mine monitoring. In *SEG Technical Program Expanded Abstracts 2018*, 4953-4957. Society of Exploration Geophysicists.

Webster, P., Wall, J., Perkins, C., and Molenaar, M. (2013). Micro-seismic detection using distributed acoustic sensing. In *SEG Technical Program Expanded Abstracts 2013*, 2459-2463. Society of Exploration Geophysicists.

Wellbrock, G. A., Xia, T. J., Huang, M.-F., Chen, Y., Salemi, M., Huang, Y.-K., Ji, P. Ip, E., and Wang, T. (2019). First Field Trial of Sensing Vehicle Speed, Density, and Road Conditions by Using Fiber Carrying High Speed Data. *Optical Fiber Communication Conference Postdeadline Papers 2019*. Optical Society of America, paper Th4C.7. DOI: doi.org/10.1364/OFC.2019.Th4C.7.

Zhou, J., Gao, D., and Zhang, D. (2007). Moving vehicle detection for automatic traffic monitoring. *IEEE transactions on vehicular technology*, 56(1), 51-59.

Tables

Table 4.1: *The velocities of the events shown in Figure 4.3.*

Event # (Time - 20:24:19)	Direction Traveling From	Velocity (m/s)	Event # (Time - 20:39:24)	Direction Traveling From	Velocity (m/s)
1	West	24	1	West	19
2	West	29	2	West	32
3	East	23	3	West	32
4	West	20	4	West	23
5	West	20	5	West	28
6	West	29	6	West	19
7	West	21	7	West	20
8	West	?	8	East	20
9	West	21	9	East	19
10	East	28	10	West	29
11	West	16			

Table 4.2: *The velocities of the events shown in Figure 4.5.*

Event # (Time - 20:24:19)	Direction Traveling From	Velocity (m/s)
1	West	25
2	West	18
3	East	16
4	West	18
5	West	22
6	West	30
7	West	28
8	West	26
9	West	30
10	West	32
11	West	36
12	West	22
13	West	35

Figures

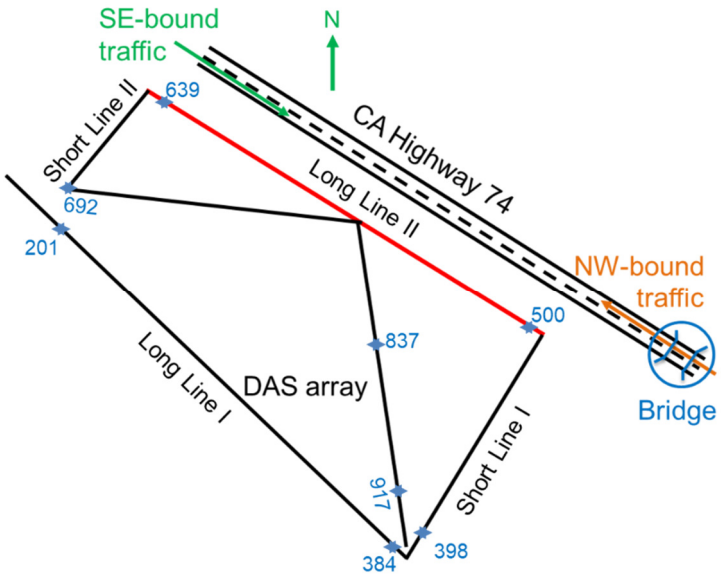

Figure 4.1: *Sketch of the DAS array study area in Garner Valley site. The stars along the DAS array indicate the channel numbers.*

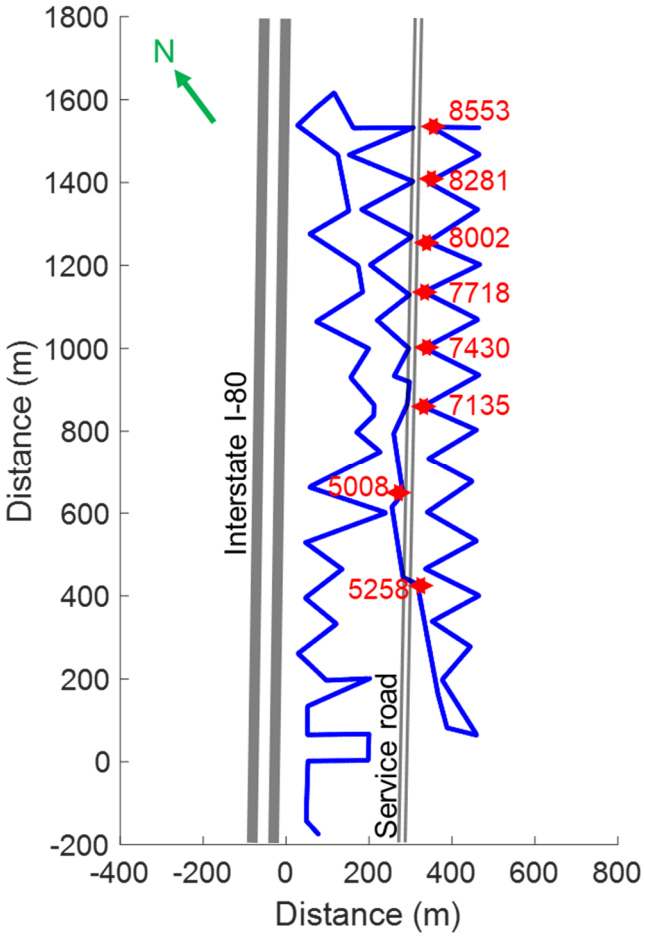

Figure 4.2: *Map of the study area in Brady Hot Springs southeast of the Interstate I-80. The blue line indicate the position of the DAS array. The red stars show the chosen channels used to monitor and calculate the speed and assess the size of the vehicles traveling along the service road.*

a)

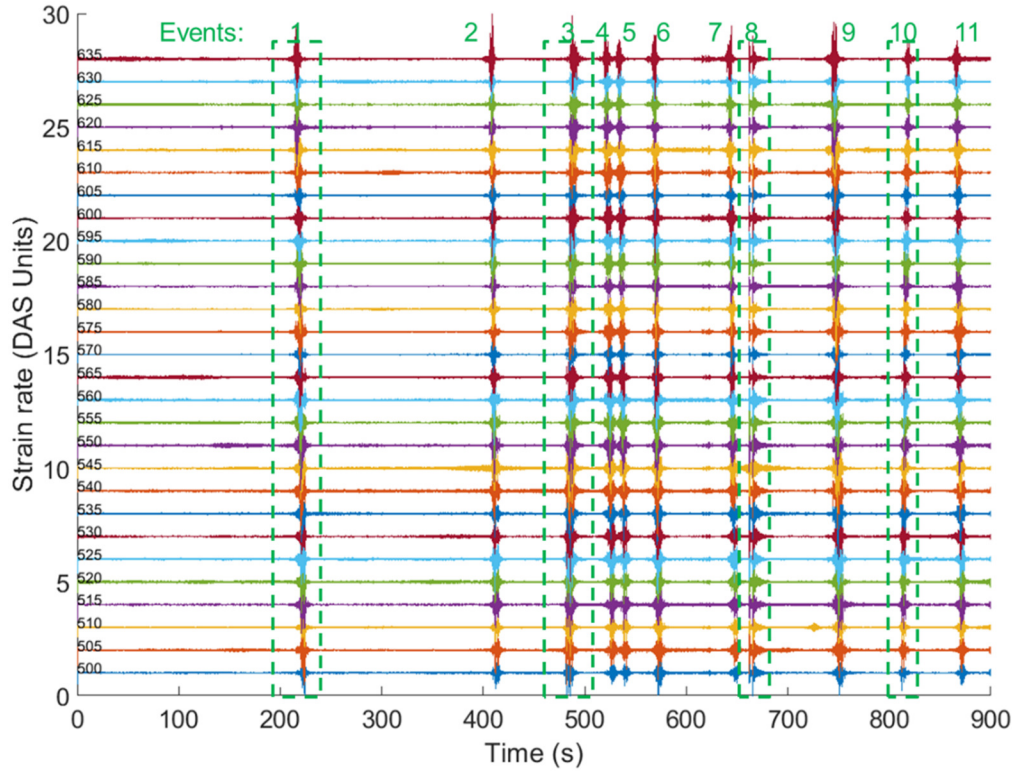

b)

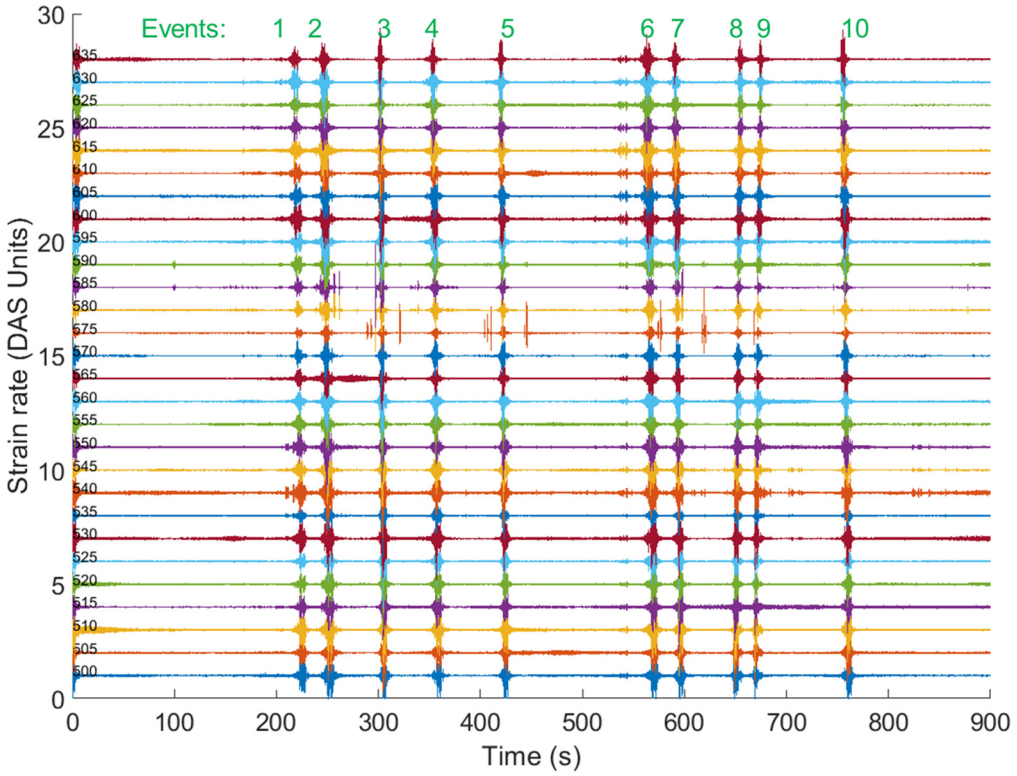

Figure 4.3: *Plot of 15 minutes of data from the DAS channel along Long Line II of the DAS array. a) Traces collected on 09/11/2016 from 8:24:19 to 8:39:19 PM local time. b) Traces collected on 09/11/2016 from 8:39:24 to 8:54:24 PM local time.*

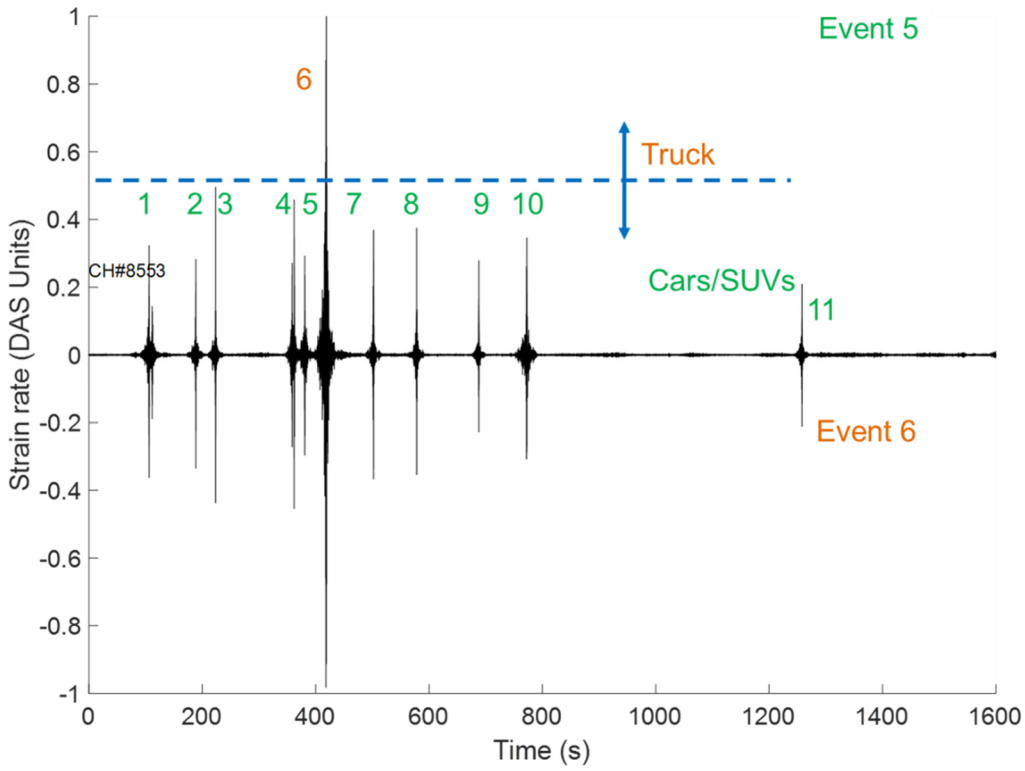

Figure 4.4: *Plot of ~27 minutes of data from the DAS channel 8553 in Brady Hot Springs. The time series was band-pass filtered between 3 and 20 Hz. The numbers from 1-11 corresponds traffic events caused by passing cars/SUVs and trucks along the service road. The 6th event corresponds to a tractor-trailer truck and the other events are from cars and SUVs. The times series was recorded on 3/17/2016 6:41:22 and 7:06:22 AM local time.*

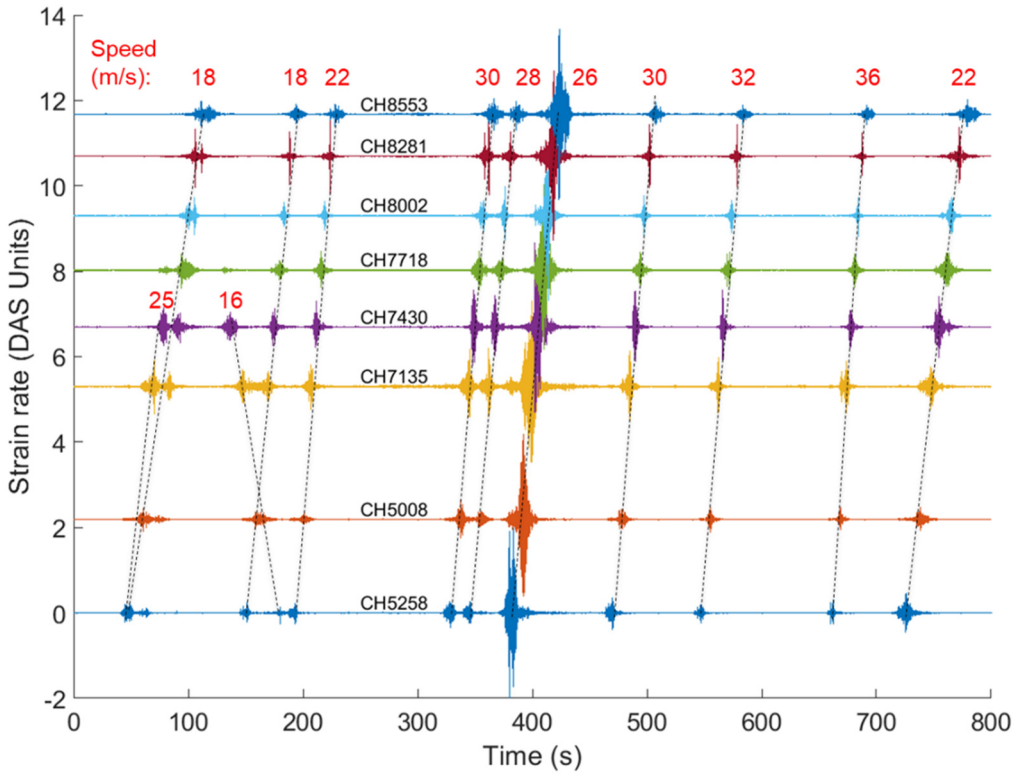

Figure 4.5: *Time series channels shown with red dots in Figure 4.2. The velocity of all vehicles varies between 16 and 36 m/s. All vehicles traveled from the SW towards the NE except for the vehicle shown labeled with speed equal to 16 m/s. The times series were recorded on 3/17/2016 6:41:22 and 7:06:22 AM local time at Brady Hot Springs.*

a)

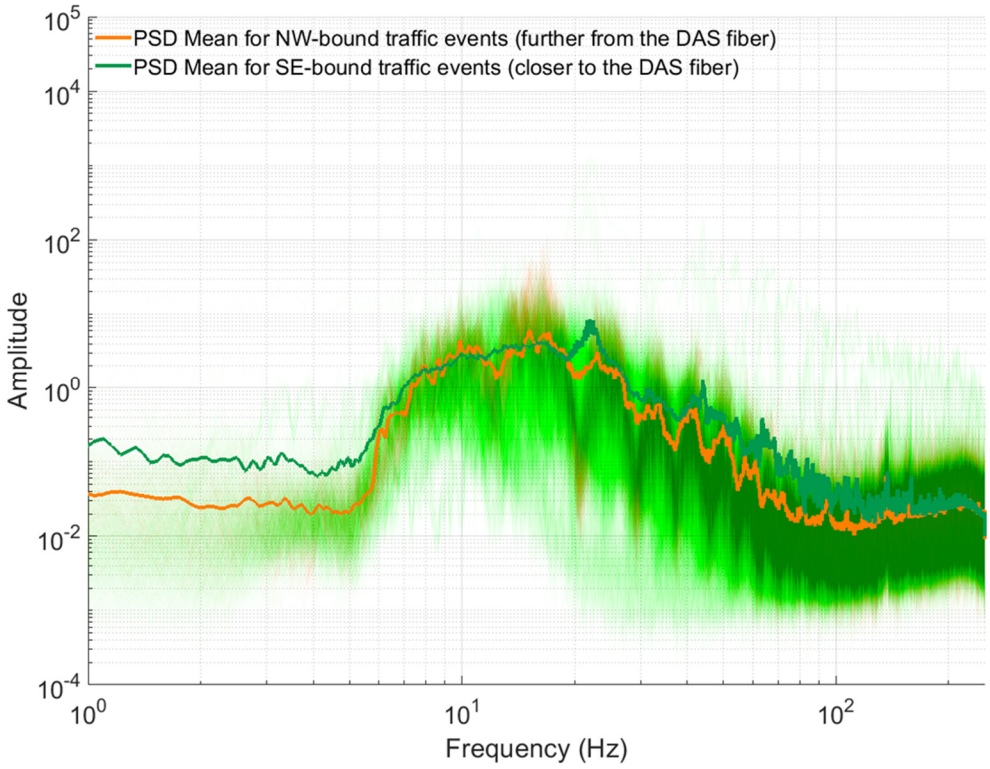

Figure 4.6: *Plot of power spectrum density of the DAS channels along the Long Line II at Garner Valley. The data corresponds to all events which presented in Figure 4.3. Effect of traffic direction of DAS responses. NW-bound traffic events (orange line) and the SE-bound traffic events (green line).*

a)

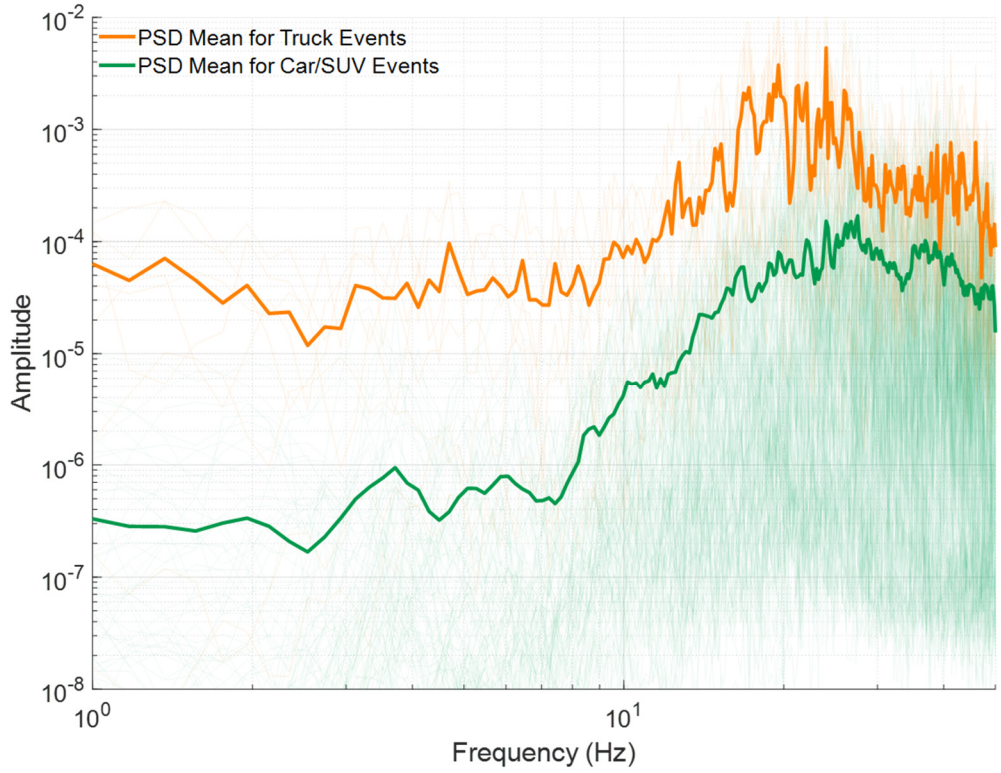

b)

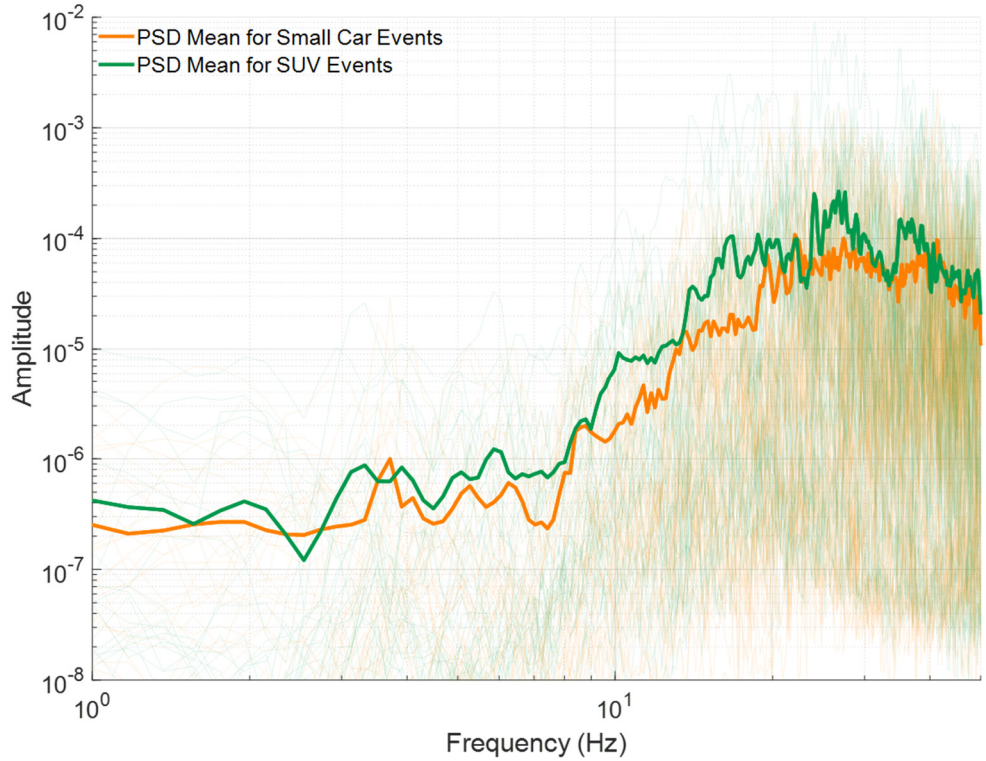

Figure 4.7: *Plots of power spectrum density of the DAS channels along the channels shown as red stars in Figure 4.2 at Brady Hot Springs. The data corresponds to all events which presented in Figure 4.4. (a) and (b) Reponses for different size of traffic. (a) Orange line and green line are the mean of the spectrum density of the truck event and of car/SUV events, respectively. (b) Orange line and green line are the mean of the spectrum density of small car events and of SUV events, respectively.*

a)

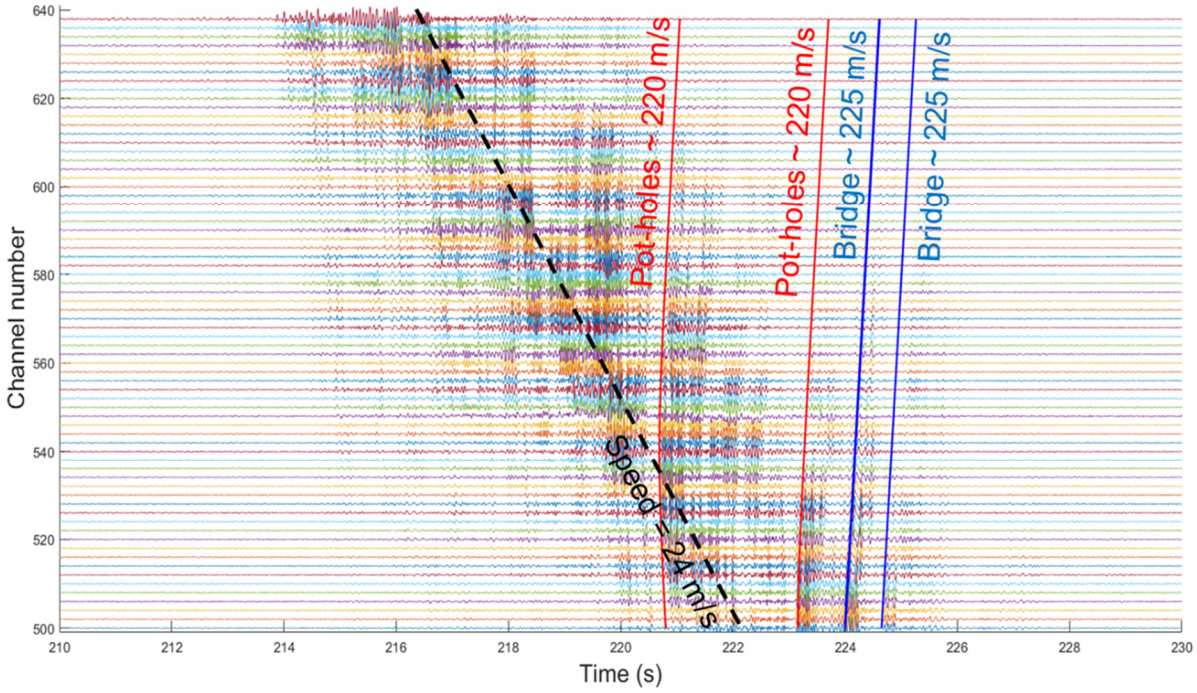
Channel number
Time (s)
Pot-holes ~ 220 m/s
Pot-holes ~ 220 m/s
Bridge ~ 225 m/s
Bridge ~ 225 m/s
Speed ~ 24 m/s

b)

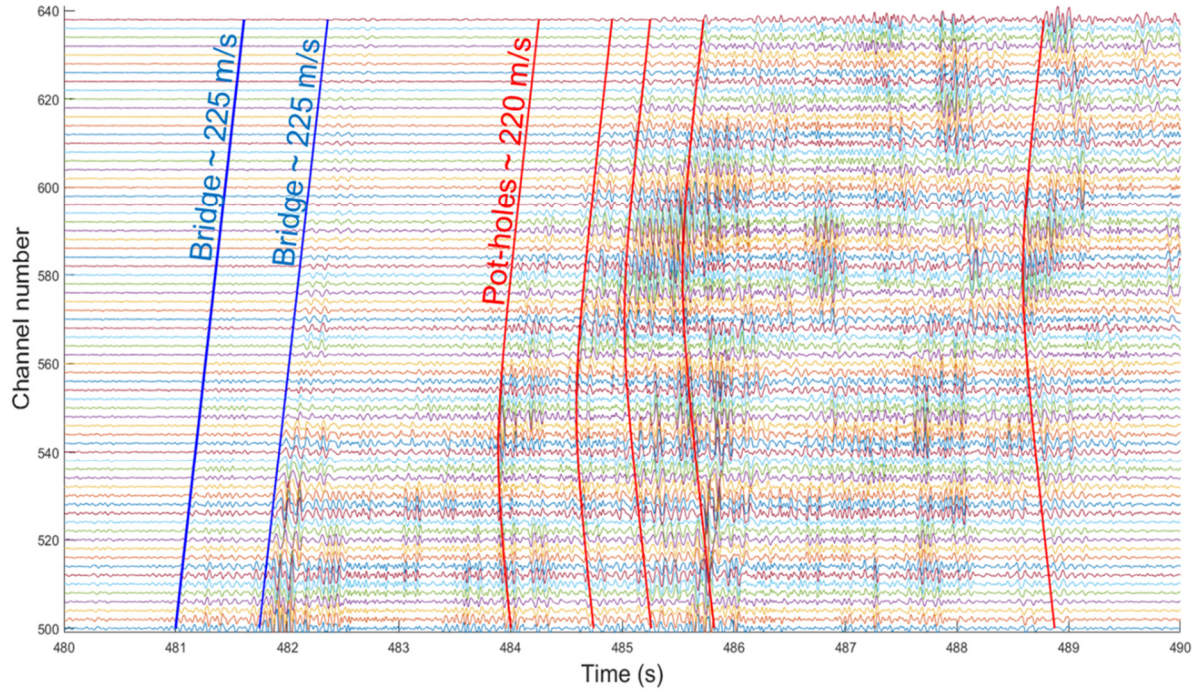
Channel number
Time (s)
Bridge ~ 225 m/s
Bridge ~ 225 m/s
Pot-holes ~ 220 m/s

c)

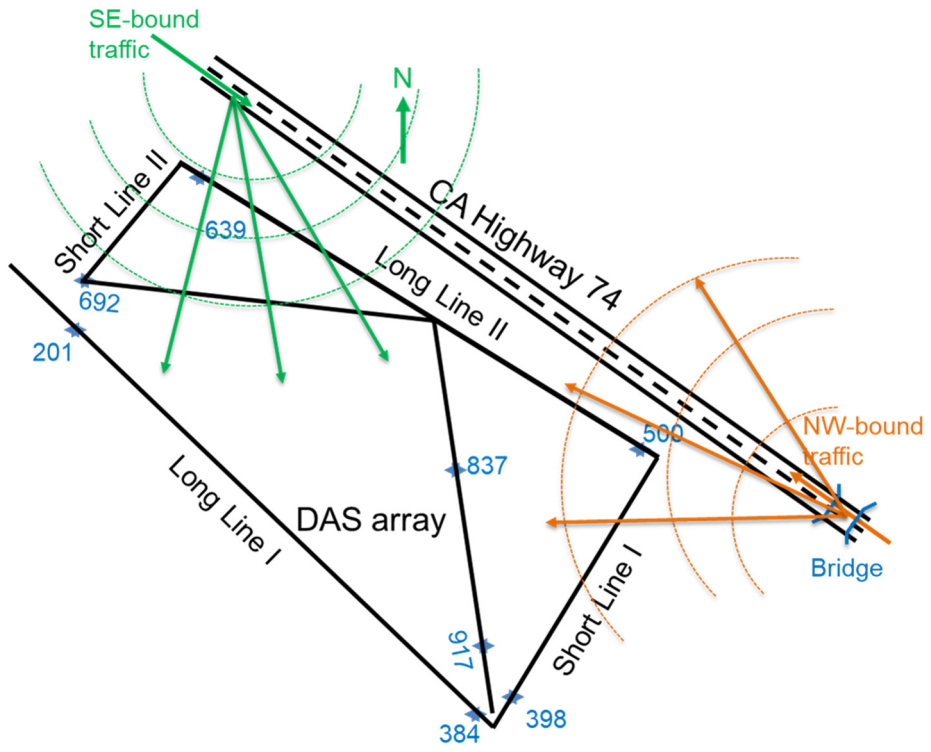

Figure 4.8: *10-s and 20-s intervals of every 15th DAS channel along the Long Line II in (a) and (b) (Figure 4.1). (a) and (b) show event 1 and 3, respectively. (a) Black positive slope indicates an SE-bound direction whose speed is 24 m/s. Red curved slopes in (a) and (b) indicate the potholes (or point source events from the roadway) whose speed is assumed 220 m/s for all of them. (c) indicate diffractions - which are sensed by Long Line II as surface waves – from vehicles hitting potholes (green) and bumps at the bridge (orange).*

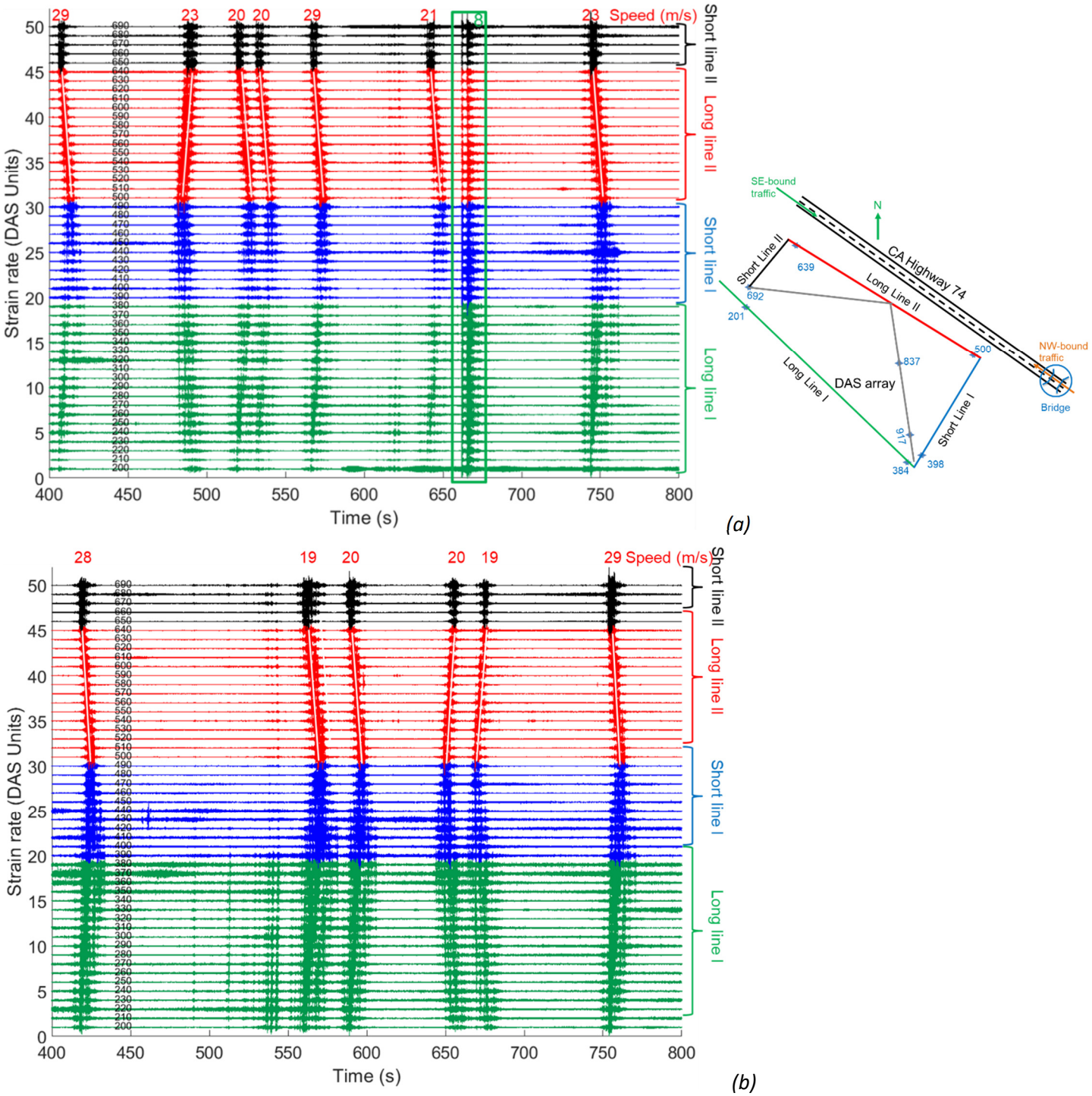

Figure 4.9: *Overview of events presented in Figure 4.3 across the whole array (see insert). Event 8 in (a) indicates an event which is not a traffic event as there is not moveout in the arrival times. For the traffic events, red numbers above each event show the speed of the vehicles.*

Chapter 5: Overall Conclusions and Engineering Implications

5.1 Summary of Results and Conclusions

In this thesis, we presented three different research studies. All these studies have in common the use of seismic arrays. We used two different types of sensor arrays: a Nodal seismometer array and a distributed acoustic sensing (DAS) array. These two arrays were deployed in the Graner Valley Down Hole Array site in Southern California and Brady Hot Springs' Enhanced Geothermal Field in Northwestern Nevada. The two sites were tested as part of the PoroTomo project, a Department of Energy's technology demonstration study for the imaging of enhanced geothermal formations.

In the first study (presented in Chapter 2), we used the analysis of polarized particle motion caused by an active Vibroseis source for the evaluation of time arrivals of P and S-waves at Brady Hot Springs. P-wave arrival times using the polarization analysis and compared to other evaluation methods (i.e., AIC picker and an energy method) and further compared with results obtained by Parker et al. (2018). The polarization direction, along with the monitoring energy in the signal amplitudes, were used to estimate the P and S-wave arrivals. The obtained arrival times show that vertical mode of Vibroseis vibration yielded the most consistent set of results as compared to the radial and transverse modes of vibrations. However, the results show an increase in the level of uncertainty for travel times longer than about 0.6 s. The methodology was then extended for the determination of S-wave arrival times. For S-wave arrival times, it was determined using the radial mode of Vibroseis vibration provided the most consistent results as compared to the vertical and transverse mode of Vibroseis vibration. However, the results also

show an increased level of uncertainty for calculated travel times longer than 1.2 s. We expect that these results will allow the additions of new datasets for the inversion analysis of the PoroTomo Laboratory at Brady Hot Springs.

The second study (presented in Chapter 3) involves the use of the Nakamura's horizontal-to-vertical spectral ratio (HVSR) method to estimate the depth to bedrock in the PoroTomo Laboratory in Brady Hot Springs. The technique uses ambient noise on 3-components geophones to calculate the HVSR response. The frequency peak of the spectral response along with the S-wave velocity of the sediments is then used to determine the depth to bedrock. However, the determination of the S-wave velocity model governs the results, and it requires a velocity calibration for the successful implementation of this technique. In this study, we used two S-wave velocity models:

- A discrete model based on the Zeng et al. (2018)'s results of ambient noise tomography (ANT) of the PoroTomo Laboratory in Brady Hot Springs. The Zeng et al.'s results yield a three-layer model at depth 10 m, 20 m, and 30 m.

- Continuous velocity models based on Hertzian's contact as presented by Santamarina et al. (2005). This model allows for the continuous calibration of the velocity profile. The velocity model was calibrated using the results from Zeng et al. (2018).

For each of the models, the original depth equation presented by Nakamura relating depth to bedrock to peak frequency and S-wave velocity was modified to capture the varying S-wave velocity distribution in the sediment layers. The applications of the discrete and continuous models shows that the Zeng et al. (2017)'s discrete S-wave velocity model show systematically

smaller depths to bedrock as compared to the results obtained with the continuous Santamarina et al. (2005)'s S-wave velocity model. The reason for these different results is that the discrete model assumes a bottom less and constant S-wave velocity third layer for the Zeng et al.'s discrete velocity model while the Santamarina et al.'s model assumes a continuously increasing S-wave velocity with depth. Those differences in the calculation of the model yields thicker layer thickness for the Santamarina et al.'s continuous S-wave velocity model.

Chapter 4 documents the final study of this thesis. For this study, DAS arrays were used to monitor traffic patterns and to assess the quality of the roadway surface at two different sites: Garner Valley and Brady Hot Springs. DAS data were able to capture the number, speed, direction, and size of vehicles along the monitored road. The data also senses the quality of the road surface. As the road surface deteriorates a more significant number of local seismic sources appear (in the form of potholes and crack on roadway surface). These types of arrays and the interpreted results could then be used by transportation engineers to continuously assess the use of the roadways and monitor the time degradation of the infrastructure.

5.2 Future Work

For future studies, the results presented in Chapter 2 for the determination of S-wave time arrivals using a polarization analysis of particle motions can be used as input to neural network algorithms to expand the investigation over the whole nodal survey array and Vibroseis locations at Brady Hot Springs for the entire period of the PoroTomo study. Next, the results from Nakamura's HVSR method can be used to add information to the 3D tomographic models of the

PoroTomo site. Lastly, the traffic signal analysis from Garner Valley and Brady Hot Springs tests sections can be extended to include the use of traffic sources as an active seismic event for the Spectral Analysis of Surface Waves (SASW) to image the near-surface at both two test sites.